A physically based distributed karst hydrological model (QMG model-V1.0) for flood simulations

Ji Li[1,*], Daoxian Yuan[1,2], Fuxi Zhang[3], Jiao Liu[4], Mingguo Ma[1]

[1]Chongqing Jinfo Mountain Karst Ecosystem National Observation and Research Station, Chongqing Key Laboratory of Karst Environment, School of Geographical Sciences, Southwest University, Chongqing 400715, China

[2]Key Laboratory of Karst Dynamics, MNR & Guangxi, Institute of Karst Geology, Chinese Academy of Geological Sciences, Guilin 541004, China

[3]College of Engineering Science and Technology, Shanghai Ocean University; Shanghai Engineering Research Center of Marine Renewable Energy 201306, China

[4]Chongqing municipal hydrological monitoring station, Chongqing 401120, China

Corresponding author: Ji Li (445776649@qq.com)

Abstract Karst trough and valley landforms are prone to flooding, primarily because of the unique hydrogeological features of karst landform, which are conducive to the spread of rapid runoff. Hydrological models that represent the complicated hydrological processes in karst regions are effective for predicting karst flooding, but their application has been hampered by their complex model structures and associated parameter set, especially so for distributed hydrological models, which require large amounts of hydrogeological data. Distributed hydrological models for predicting the flooding is highly dependent on distributed modeling, complicated boundary parameters setting, and tremendous hydrogeological data processing that is both time and computational power consuming. Proposed here is a distributed physically-based karst hydrological model, known as the

QMG (Qingmuguan) model. The structural design of this model is relatively simple, and it is generally divided into surface and underground double-layered structures. The parameters that represent the structural functions of each layer have clear physical meanings, and the parameters are less than those of the current distributed models. This allows modeling in karst areas with only a small amount of necessary hydrogeological data. 18 flood processes across the karst underground river in the Qingmuguan karst trough valley are simulated by the QMG model, and the simulated values agree well with observations, for which the average value of Nash–Sutcliffe coefficient was 0.92. A sensitivity analysis shows that the infiltration coefficient, permeability coefficient, and rock porosity are the parameters that require the most attention in model calibration and optimization. The improved predictability of karst flooding by the proposed QMG model promotes a better mechanistic depicting of runoff generation and confluence in karst trough valleys.

Keywords: Simulation and forecasting of karst floods; Karst trough valleys; QMG (Qingmuguan) model; Parametric optimization; Parameter sensitivity analysis

1 Introduction

Karst trough and valley landforms are very common in China, especially in the southwest. In general, these karst areas are water scarce during most of the year because their surfaces store very little rainfall, but they are also potential birthplaces for floods because trough and valley landforms and topographic features facilitate the formation and propagation of floods (White, 2002; Li et al., 2021). The coexistence of drought and flood is a typical phenomenon in these karst trough and valley areas. Taking the example of the present study area, i.e. the Qingmuguan karst trough valley, floods used to happen here constantly during the rainy season. In recent years, with more extreme rainfall events and the increased area of construction land in the region, rainfall infiltration has decreased and rapid runoff over

47 impervious surfaces has increased, resulting in frequent catastrophic flooding in the basin

48 (Liu et al., 2009). Excess water overflows from karst sinkholes and underground river

49 outlets often occur during floods (Jourde et al., 2007, 2014; Martinotti et al., 2017), flooding

50 large areas of farmland and residential areas and causing serious economic losses (Gutierrez,

51 2010; Parise, 2010; Yu et al., 2020). Therefore, it is both important and urgent to simulate

52 and predict karst flooding events in karst trough and valleys such as the study area.

53   Hydrological models can be effective for forecasting floods and evaluating water

54 resources in karst areas (Bonacci et al., 2006; Ford and Williams, 2007; Williams, 2008,

55 2009). However, modelling floods in karst regions is extremely difficult because of the

56 complex hydrogeological structure. Karst water-bearing systems consist of multiple media

57 under the influence of complex karst development dynamics (Worthington et al., 2000;

58 Kovács and Perrochet, 2008; Gutierrez, 2010), such as karst caves, conduits, fissures and

59 pores, and are usually highly spatially heterogeneous (Chang and Liu, 2015; Teixeiraparente

60 et al., 2019). In addition, the intricate surface hydrogeological conditions and the

61 hydrodynamic conditions inside the karst water-bearing medium result in significant

62 temporal and spatial differences in the hydrological processes in karst areas (Geyer et al.,

63 2008; Bittner et al., 2020).

64   In early studies of flood forecasting in karst regions, simplified lumped hydrological

65 models were commonly used to describe the rainfall–discharge relationship (e.g. Kovács and

66 Sauter, 2007; Fleury et al., 2007b; Jukić and Denić, 2009; Hartmann et al., 2014a). With the

67 development of physical exploration technology and the progress made in mathematics,

68 computing and other interdisciplinary disciplines, the level of modelling has gradually

69 improved (Hartmann and Baker, 2017; Hartmann, 2018; Petrie et al., 2021), and distributed

70 hydrological models have subsequently become widely used in karst areas. The main

71 difference between lumped and distributed hydrological models is that the latter divide the

72 entire basin into many sub-basins to calculate the runoff generation and confluence, thereby

73 better describing the physical properties of the hydrological processes inside the karst

74 water-bearing system (Jourde et al., 2007; Hartmann, 2018; Epting et al., 2018).

75   Because of their simple structure and little demand for modelling data, lumped

hydrological models have been used widely in karst areas (Kurtulus and Razack, 2007; Ladouche et al., 2014). In a lumped model, the river basin is considered as a whole to calculate the runoff generation and confluence, and there is no division running into sub-basins (Dewandel et al., 2003; Bittner et al., 2020). Lumped models usually consider the inputs and outputs of the model (Liedl and Sauter, 2003; Hartmann and Bake, 2013, 2017). In addition, most of the model parameters are not optimized in a lumped model, and the physical meaning of each parameter is unclear (Chen, 2009; Bittner et al., 2020).

Distributed hydrological models are of active interest in flood simulation and forecasting research (Ambroise et al., 1996; Beven and Binley, 2006; Zhu and Li, 2014). Compared with a lumped model, a distributed model has a more definite physical significance for the model structure in terms of its mechanism (Meng and Wang, 2010; Epting et al., 2018). In a distributed hydrological model, an entire karst basin can be divided into many sub-basins (Birk et al., 2005) using high-resolution digital elevation map (DEM) data. In the rainfall-runoff algorithm of the model, the hydrogeological conditions and karst aquifer characteristics can be considered fully to simulate precisely the runoff generation and confluence (Martinotti et al.,2017; Gang et al., 2019). The commonly used basin distributed hydrological models (i.e. not a special groundwater numerical model such as MODFLOW) have also been applied widely in karst areas and include the SHE/MIKE SHE model (Abbott et al., 1986a,b; Doummar et al., 2012), SWMM model (Peterson and Wicks, 2006; Blansett and Hamlett, 2010; Blansett, 2011), TOPMODEL (Ambroise et al., 1996; Suo et al., 2007; Lu et al., 2013; Pan, 2014) and SWAT model (Peterson and Hamlett, 1998; Ren, 2006).

The commonly used distributed hydrological models have multiple structures and numerous parameters (Lu et al., 2013; Pan, 2014), which means that a distributed model may need vast amounts of data to build its framework in karst regions. For example, the distributed groundwater model MODFLOW-CFPM1 requires detailed data regarding the distribution of karst conduits in a study area (Reimann et al., 2009). Another example is the Karst–Liuxihe model (Li et al., 2019), there are fifteen parameters and five underground vertical structures in the model.Such a complex structure makes the modeling data demand

105   is large, and the modeling in karst area is extremely difficult. In addition, a special borehole

106   pumping test may be required to obtain the rock permeability coefficient.

107   To overcome the difficulty of the large modelling-data demands for distributed hydrological

108   models in karst areas, a new physically based distributed hydrological model—known as the

109   QMG (Qingmuguan) model-V1.0—was developed in the present study. Other commonly

110   used karst groundwater models with complex structure and parameters—such as the

111   aforementioned MODFLOW-CFPM1 model—require a lot of hydrogeological data for

112   modelling in karst areas (Qin and Jiang, 2014). The new QMG model has a high potential

113   for application in karst hydrological simulation and forecasting. It has certain advantages in

114   its framework and structural design, having a double-layer structure and fewer parameters.

115   The horizontal structure is divided into river channel units and slope units, and the vertical

116   structure below the surface is divided into a shallow karst aquifer and a deep karst aquifer

117   system. This relatively simple model structure reduces the demand for modelling data in

118   karst areas, and only a small amount of hydrogeological data is needed for modelling. To

119   ensure that the QMG model works well in karst flood simulation and prediction despite its

120   relatively simple structure and parameters, we carefully designed the algorithms for runoff

121   generation and confluence in the model. Also, to verify the applicability of the QMG model

122   to flood simulation in karst basins, we selected the Qingmuguan karst trough valley in

123   Chongqing, China as the study area for a flood simulation and uncertainty analysis. In

124   particular, we analysed the sensitivity of the model parameters.

125   **2   Study area and data**

126   **2.1 Landform and topography**

127   The Qingmuguan karst trough valley is located in the southeastern part of the Sichuan Basin,

128   China at the junction of the Beibei and Shapingba districts in Chongqing, with the

129   coordinates of 29°40′N–29°47′N, 106°17′E–106°20′E. The basin covers an area of 13.4 km^2

130   and is part of the southern extension of the anticline at Wintang Gorge in the Jinyun

131   Mountains, with the anticlinal axis of Qingmuguan located in a parallel valley in eastern

132 Sichuan (Yang et al., 2008). The surface of the anticline is heavily fragmented, and faults

133 are extremely well developed with large areas of Triassic carbonate rocks exposed. Under

134 the long-term erosion of karst water, a typical karst trough landformshas formed (Liu et al.,

135 2009). This karst trough landform provides convenient conditions for flood propagation, and

136 the development of karst landforms is extremely common in the karst region of southwest

137 China, especially in the karst region of Chongqing.

138 The basin is oriented in a narrow band of slightly curved arcs and is ~12 km long from

139 north to south. The direction of the mountains in the region is generally consistent with the

140 direction of the tectonic line. The map in Figure 1 gives an overview of the Qingmuguan

141 karst basin.

142 **Figure 1.** The Qingmuguan karst basin.

143 **2.2 Hydrogeological conditions**

144 The Qingmuguan basin is located within the subtropical humid monsoon climate zone, with

145 an average temperature of 16.5 ℃ and an average precipitation of 1250 mm concentrated

146 mainly in May–September. An underground river system has developed in the karst trough

147 valley, with a length of 7.4 km, and the water supply of the underground river is mainly

148 rainfall recharge (Zhang, 2012). Most of the precipitation is collected along the hill slope

149 into the karst depressions at the bottom of the trough valley, where it is recharged to the

150 underground river through the dispersed infiltration of surface karst fissures and sinkholes

151 (Fig. 1a). An upstream surface river collects in a gentle valley and enters the underground

152 river through the Yankou sinkhole (elevation 524 m). Surface water in the middle and lower

153 reaches of the river system enters the underground river system mainly through cover

154 collapse sinkholes (Gutierrez et al., 2014) or fissures.

155 The stratigraphic and lithologic characteristics of the basin are dominated largely by

156 carbonate rocks of the Lower Triassic Jialingjiang Group (T_{1j}) and Middle Triassic Leikou

157 Slope Group (T_{2l}) on both sides of the slope, with some quartz sandstone and mudstone

158 outcrops of the Upper Triassic Xujiahe Group (T_{3xj}) (Zhang, 2012). The topography of the

159   basin presents a general anticline (Fig. 1b), where carbonate rocks on the surface are

160   corroded and fragmented, high permeability. Compared with the core of the anticline, the

161   shale of the anticline are less eroded and form a good waterproof layer.

162   To investigate the distribution of karst conduits in the underground river system, we

163   conducted a tracer test in the study area. The tracer was placed into the Yankou sinkhole and

164   recovered in the Jiangjia spring (Fig. 1a,c). According to the tracer test results (Gou et al.,

165   2010), the karst water-bearing medium in the aquifer was anisotropic, and the karst conduits

166   in the underground river were extremely well developed, and there was a large

167   single-channel underground river about five meters wide. The response of the underground

168   river to rainfall was very fast, with the peak flow observed at the outlet of Jiangjia spring

169   6–8 h after rainfall based on the tracer test results. The flood peak rose quickly and the

170   duration of the peak flow was short. The underground river system in the study area is

171   dominated by large karst conduits, which is not conducive to water storage in water-bearing

172   media, but is very conducive to the propagation of floods.

173   **2.3 Data**

174   To build the QMG model to simulate the karst flood events, the necessary modelling

175   baseline data had to be collected, including: 1) high-resolution DEM data and

176   hydrogeological data (e.g., the thickness of the epikarst zone, rainfall infiltration coefficient

177   on different karst landforms, and permeability coefficient of rock); 2) land-use and soil type

178   data; and 3) rainfall data in the basin and water flow data of the underground river. The

179   DEM data was downloaded from a free database on the public Internet, with an initial spatial

180   resolution of 30 $\times$ 30 m. The spatial resolution of landuse and soil types were 1000 $\times$ 1000

181   m, and they were also downloaded from the Internet. After considering the applicability of

182   modelling and computational strength, as well as the size of the basin in the study area (13.4

183   km^2), the spatial resolution of the three types of data was resampled uniformly in the QMG

184   model and downscaled to 15 $\times$ 15 m based on a spatial discrete method by Berry et. (2010).

185   The hydrogeological data necessary for modelling was obtained in three simple ways. 1)

186   A basin survey was conducted to obtain the thickness of the epikarst zone, which was

187 achieved by observing the rock formations on hillsides following cutting for road

188 construction. Information was collected regarding the location, general shape, and size of

189 karst depressions and sinkholes, which had a significant impact on compiling the DEM data

190 and determining the convergence process of surface runoff. And the sinkholes in the basin

191 are cover collapse sinkholes (Gutierrez et al., 2014) according to the basin survey. There are

192 3 large sinkholes (more than 3 meters in diameter) and 12 small sinkholes less than 1 meter

193 in diameter.   The rest of the sinkholes between 1 and 3 meters in diameter are 5 in total.

194 The confluence calculation of these sinkholes in the model was based on the results of

195 previous study (Meng et al., 2009). 2) Empirical equations developed for similar basins were

196 used to obtain the rainfall infiltration coefficient for different karst landforms and the

197 permeability coefficient of rock. For example, the rock permeability coefficient was

198 calculated based on an empirical equation from a pumping test in a coal mine in the study

199 area (Li et al., 2019). 3) A tracer experiment was conducted in the study area (Gou et al.,

200 2010) to obtain information on the underground river direction and flow velocity, for

201 instance, underground karst conduits are well developed in the area, which form an

202 underground river about five meters wide. There is no hydraulic connection between the

203 underground river system in the area and the adjacent basin, means there is no overflow

204 recharge.

205   Rainfall and flood data are important model inputs, and represent the driving factors

206 that allow hydrological models to operate. In the study area, rainfall data was acquired by

207 two rain gauges located in the basin (Fig. 1a). Point rainfall was then spatially interpolated

208 into basin-level rainfall (for such a small basin area rainfall results obtained from two rain

209 gauges was considered representative). There were 18 karst flood events in the period of 14

210 April 2017 to 10 June 2019. We built a rectangular open channel at the underground river

211 outlet and set up a river gauge on it (Fig. 1a) to record the water level and flow data every 15

212 minutes.

3 Methodology

3.1 Hydrological model framework and algorithms

The hydrological model developed in this study was named the QMG model after the basin for which it was developed and to which it was first applied, i.e. the Qingmuguan basin. The QMG model has a two-layer structure, including a surface part and an underground part. The surface structure mainly performing the calculation of runoff generation and the confluence of the surface river, while the underground structure   performs the confluence calculation of the underground river system.

The structure of the QMG model is divided into a two-layer structure, both horizontally and vertically. The horizontal structure of the model is divided into river channel units and slope units. The vertical structure below the surface is divided into a shallow karst aquifer (including soil layers, karst fissures and conduit systems in the epikarst zone) and a deep karst aquifer system (bedrock and underground river system). This relatively simple model structure means that only a small amount of hydrogeological data is needed in karst regions. Figure 2 shows a flowchart of the modelling and calculation procedures required for the QMG model.

Figure 2. Modelling flow chart of QMG (Qingmuguan) model.

To describe accurately the runoff generation and confluence on a grid scale, these karst sub-basins are further divided into many karst hydrological response units (KHRUs) based on the high-resolution (15 × 15 m) DEM data in the model. The specific steps involved in the division were adopted by referring to studies of hydrological response units (HRUs) in TOPMODEL by Pan (2014). As the smallest basin computing units, the KHRUs can effectively ignore the spatial differences of karst development within the units and reduce the uncertainty in the classification of model units. Figure 3 shows the spatial structure of the KHRUs.

Figure 3. Spatial structure of karst hydrological response units (KHRUs) (Li et al., 2021).

The right-hand side of Figure 3 shows a three-dimensional spatial model of KHRUs established in the laboratory to reflect visually the storage and movement of water in the

241 karst water-bearing medium with each spatial anisotropy, and to provide technical support

242 for establishing the hydrological model.

243   The modelling and operation of the QMG model consists of three main stages: 1)

244 spatial interpolation, and the retention of rainfall and evaporation calculations; 2) runoff

245 generation and confluence calculation for the surface river; and 3) confluence calculation for

246 the underground runoff, including the confluence in the shallow karst aquifer and the

247 underground river system.

248 **3.1.1 Rainfall and evaporation calculation**

249 In the QMG model, the spatial interpolation of rainfall is accomplished by a kriging method

250 using the ArcGIS 10.2 software. The Tyson polygon method may be a simpler method for

251 rainfall interpolation if the number of rainfall gauges in the basin is sufficient. The point

252 rainfall observed by the two rainfall gauges in the basin (Fig. 1a) was interpolated spatially

253 into areal rainfall for the entire basin.

254   Basin evapotranspiration in the KHRUs was mainly vegetal, soil evaporation and water

255 surface evaporation. They were calculated using the following equations (modified from Li

256 et al., 2020):

257
$$
\begin{cases}
E_v = V^{t+\Delta t} - V^t - P_v \\
E_s = \lambda E_p, \text{if } F = F_c \\
E_s = \lambda E_p \dfrac{F}{F_c}, \text{if } F < F_{sat} \\
E_w = \Delta e \cdot \left[1.12 + 0.62(\Delta T)^{0.9}\right] \cdot \left[0.084 + 0.24\left(1 - \gamma^2\right)^{1/2}\right] \cdot \left[0.348 + 0.5\omega^{1.8 - 1.137\omega^{0.05}}\right]
\end{cases}
\tag{1}
$$

258 Here, E_v [mm] is the vegetal discharge, $V^{t+\Delta t} - V^t$ [mm] is the rainfall variation by

259 vegetation interception, P_v [mm] is the vegetation interception of rainfall and E_s [mm]

260 is the actual soil evaporation. The term λ is the evaporation coefficient. The term E_p

261 [mm] is the evaporation capability, which can be measured experimentally or estimated

262 by the water surface evaporation equation E_w. The term F [mm] is the actual soil

263 moisture, F_{sat} [mm] is the saturation moisture content, F_c [mm] is the field capacity, E_w

264 [mm/d] is the evaporation of the water surface and $\Delta e = e_0 - e_{150}$ [hPa] is the draught

265   head between the saturation vapour pressure of the water surface and the air vapour

266   pressure 150 m above the water surface. The term $\Delta T = t_0 - T_{150}$ [℃] is the temperature

267   difference between the water surface and the temperature 150 m above the water

268   surface, γ is the relative humidity 150 m above the water surface and ω [m/s] is the

269   wind speed 150 m above the water surface.

3.1.2 Runoff generation

271   In the QMG model, the surface runoff generation in river channel units means the rainfall in

272   the river system after deducting evaporation losses. This portion of the runoff will

273   participate in the confluence process directly through the river system, rather than

274   undergoing infiltration. In contrast, the process of runoff generation in slope units is more

275   complex, and its classification is related to the developmental characteristics of surface karst

276   in the basin, rainfall intensity and soil moisture. For example, when the soil moisture content

277   is already saturated, there is the potential for excess infiltration surface runoff in exposed

278   karst slope units. The surface runoff generation of the KHRUs in the river channel units and

279   slope units can be described by the following equations (modified from Chen, 2009, 2018;

280   Li et al., 2020):

$$
\begin{cases}
P_r(t) = \left[P_i(t) - E_p \right] \dfrac{L \cdot W_{max}}{A} \\
R_{si} = (P_i - f_i), P_i \geq f_{max} \\
R_{si} = 0, P_i < f_{max} \\
f_{max} = \alpha(F_c - F)^\beta + F_s
\end{cases}
\tag{2}
$$

282   Here, $P_r(t)$ [mm] is the net rainfall (deducting evaporation losses) in the river channel units

283   at time t [h], $P_i(t)$ [mm] is the rainfall in the river channel units, L [m] is the length of the

284   river channel, W_{max} [m] is the maximum width of the river channel selected and A [m^2] is

285   the cross-sectional area of the river channel. R_{si} [mm] is termed the excess infiltration runoff

286   in the QMG model, when the vadose zone is short of water and has not been filled. The

287   infiltration capacity f_{max} is different in different karst landform units, α, β are the parameters

288   of the Holtan model and F_s [mm] is the stable depth of soil water infiltration.

289   In the KHRUs (Fig. 3), underground runoff is generated primarily from the infiltration

290   of rainwater and direct confluence recharge from sinkholes or skylights. In the QMG model,

291   the underground runoff is calculated by the following equations (modified from Chen,

292   2018):

293

$$\begin{cases} R_g = R_0 \exp(-pt^m) \\ R_e = v_e \cdot I_w \cdot z \end{cases} \tag{3}$$

294   where

295

$$\begin{cases} \dfrac{\partial R_e}{\partial x} + I_w \cdot z \cdot \dfrac{\partial F}{\partial t} = R_r - R_{epi} \\ v_e = K \cdot \tan(\alpha), \quad F > F_c \\ v_e = 0, \quad F \le F_c \end{cases} \tag{4}$$

296   Here, R_g [mm] is the underground runoff depth (this part of the underground runoff is mainly

297   from the direct confluence supply of the karst sinkholes or karst windows in the study area),

298   R_0 [mm] is the average depth of the underground runoff, p and m are attenuation coefficients

299   calculated by conducting a tracer test in the study area, R_e [L/s] is the underground runoff

300   generated from rainfall infiltration in the epikarst zone, I_w [mm] is the width of the

301   underground runoff on the KHRUs, z [mm] is the thickness of the epikarst zone, R_r [mm^2/s]

302   is the runoff recharge on the KHRUs during period t, R_{epi} [mm^2/s] is the water infiltration

303   from rainfall, v_e [mm/s] is the flow velocity of the underground runoff, K [mm/s] is the

304   current permeability coefficient and α is the hydraulic gradient of the underground runoff.

305   If the current soil moisture is less than the field capacity, i.e. $F \le F_c$, then the vadose zone

306   is not yet full, there will be no underground runoff generation, and rainfall infiltration at this

307   time will continue to compensate for the lack of water in the vadose zone until it is full and

308   before runoff is generated.

309   **3.1.3 Channel routing and confluence**

310   In the QMG model, the calculation of runoff confluence on the KHRUs includes the

311   confluence of surface river channel and underground runoff. There are already many mature

312   and classical algorithms available for calculating the runoff confluence in river channel units

313 and slope units, such as the Saint-Venant equations and Muskingum convergence model. In

314 this study, the Saint-Venant equations were adopted to describe the confluence in the surface

315 river and hill slope units, for which a wave movement equation was adopted to calculate

316 confluence in slope units (Chen, 2009):

317
$$\begin{cases} \dfrac{\partial Q}{\partial x} + L \dfrac{\partial h}{\partial t} = q \\ S_f - S_0 = 0 \end{cases} \tag{5}$$

318 where

319
$$Q = vhL = \dfrac{L}{n} h^{\frac{5}{3}} S_0^{\frac{1}{2}} . \tag{6}$$

320 Here, we customized two variables a and b:

321
$$\begin{cases} a = (\dfrac{n}{L} S_0^{-\frac{1}{2}})^{\frac{3}{5}} \\ b = \dfrac{3}{5} \end{cases} \tag{7}$$

322 Equation (7) was substituted into Eq. (5) and discretized by a finite-difference method,

323 giving

324
$$\begin{cases} \dfrac{\partial Q}{\partial x} + abQ^{(b-1)} \dfrac{\partial Q}{\partial t} - q = 0 \\ \dfrac{\Delta t}{\Delta x} Q_{i+1}^{t+1} + a(Q_{i+1}^{t+1})^b = \dfrac{\Delta t}{\Delta x} Q_i^{t+1} + a(Q_{i+1}^t)^b + q_{i+1}^{t+1} \Delta t \end{cases} \tag{8}$$

325 The Newton–Raphson method was used for the iterative calculation using Eq. (8):

326
$$\left[Q_{i+1}^{t+1} \right]^{k+1} = \left[Q_{i+1}^{t+1} \right]^k - \dfrac{\dfrac{\Delta t}{\Delta x} \left[Q_{i+1}^{t+1} \right]^k + a(\left[Q_{i+1}^{t+1} \right]^k)^b - \dfrac{\Delta t}{\Delta x} Q_i^{t+1} - a(Q_{i+1}^t)^b - q_{i+1}^{t+1} \Delta t}{\dfrac{\Delta t}{\Delta x} + ab(\left[Q_{i+1}^{t+1} \right]^k)^{b-1}} , \tag{9}$$

327 where Q [L/s] is the confluence of water flow in slope units, L [dm] is its runoff width, h

328 [dm] is the runoff depth and q [dm^2/s] is the lateral inflow on the KHRUs. Here, the friction

329 slope S_f equals the hill slope S_0, and the inertia term and the pressure term in the motion

330 equation of the Saint-Venant equations were ignored. The term v [dm/s] is the flow velocity

331 of surface runoff in the slope units as calculated by the Manning equation, n is the roughness

332 coefficient of the slope units, Q_i^{t+1} [L/s] is the slope inflow in the KHRU at time $t+1$ and

333 Q_{i+1}^{t+1} [L/s] is the slope discharge in the upper adjacent KHRU at time $t+1$.

334 Similarly, the surface river channel confluence was described based on the

335 Saint-Venant equation, where a diffusion wave movement equation was adopted, meaning

336 that the inertia term in the motion equation was ignored:

337
$$\begin{cases} \dfrac{\partial Q}{\partial x} + \dfrac{\partial A}{\partial t} = q \\ S_f = S_0 - \dfrac{\partial h}{\partial x} \end{cases} \tag{10}$$

338 A finite-difference method and the Newton–Raphson method were used for the iterative

339 calculation   of   the   above   equation:

340
$$\begin{cases} \left[Q_{i+1}^{t+1} \right]^{k+1} = \left[Q_{i+1}^{t+1} \right]^{k} - \dfrac{\dfrac{\Delta t}{\Delta x}\left[Q_{i+1}^{t+1} \right]^{k} + c(\left[Q_{i+1}^{t+1} \right]^{k})^{b} - \dfrac{\Delta t}{\Delta x} Q_i^{t+1} - c(Q_{i+1}^t)^b - q_{i+1}^{t+1}\Delta t}{\dfrac{\Delta t}{\Delta x} + cb(\left[Q_{i+1}^{t+1} \right]^{k})^{b-1}} \\ c = (\dfrac{1}{3600} n\chi^{\frac{2}{3}} S_f^{-\frac{1}{2}})^{\frac{3}{5}} \end{cases} \tag{11}$$

341 where Q [L/s] is the water flow in surface river channel units, A [dm^2] is the discharge

342 section area, c is a custom intermediate variable and χ [dm] is the wetted perimeter of the

343 discharge section area.

344 The underground runoff in the model includes the confluence of the epikarst zone and

345 underground river. In the epikarst zone, the karst water-bearing media are highly

346 heterogeneous (Williams, 2008). For example, the anisotropic karst fissure systems and

347 conduit systems consist of the corrosion fractures. When rainfall infiltrates into the epikarst

348 zone, water moves slowly through the small (less than 10cm in this study) karst fissure

349 systems, while it flows rapidly in larger (more than 10cm) conduits. The key to determining

350 the confluence velocity lies in the width of karst fractures. In the KHRUs (Fig. 3), the 10-cm

351 width of the fracture was used as a threshold value (Atkinson, 1977) based on the borehole

352 pumping test in the basin, meaning that if the fracture width exceeded 10 cm, then the water

353 movement into it was defined as rapid flow; otherwise, it was defined as slow flow. The

354 confluence in the epikarst zone was calculated by the following equation (modified from

355 Beven and Binley, 2006):

$$Q(t)_{ijk} = b_{ijk} \cdot \frac{\Delta h}{\Delta l} R_i C_j \cdot T(t)_{\text{slow/rapid}} \tag{12}$$

357 where

$$
\begin{cases}
T(t)_{\text{slow}} = nr \dfrac{\rho g R_i C_j L_k}{12 v} \\[2mm]
T(t)_{\text{rapid}} = \dfrac{K_{ij}\left(e^{-f_{ij}h_{ij}} - e^{-f_{ij}z_{ij}}\right)}{f_{ij}}
\end{cases}
\tag{13}
$$

359 Here, $Q(t)_{ijk}$ [L/s] is the flow confluence in the epikarst zone at time t, b_{ijk} [dm] is the

360 runoff width, $\dfrac{\Delta h}{\Delta l}$ is the dimensionless hydraulic gradient, $T(t)_{\text{slow/rapid}}$ is the

361 dimensionless hydraulic conductivity, ρ [g/L] is the density of the water flow, g [m/s^2] is

362 gravitational acceleration, n is the valid computational units, $R_i C_j L_k$ [L] is the volume of

363 the ijk-th KHRU, v is the kinematic viscosity coefficient, f_{ij} is the attenuation coefficient in

364 the epikarst zone, h_{ij} [dm] is the depth of shallow groundwater and z_{ij} [dm] is the thickness

365 of the epikarst zone.

366   The distinction between rapid and slow flows in the epikarst zone is not absolute. The

367 10-cm width of a karst fracture as the dividing threshold is underrepresented due to the only

368 five limited boreholes have been tested for pumping in the region. In fact, there is usually

369 water exchange between the rapid and slow flows at the junction of large and small fissures

370 in karst aquifers. In the QMG model, this water exchange can be described with this

371 equation (modified form Li et al., 2021):

$$
\begin{cases}
Q = \alpha_{i,j,k}\left(h_n - h_{i,j,k}\right) \\[2mm]
\alpha_{i,j,k} = \displaystyle\sum_{ip=1}^{np} \dfrac{\left(K_w\right)_{i,j,k} \pi d_{ip} \frac{1}{2}\left(\Delta l_{ip} \tau_{ip}\right)}{r_{ip}}
\end{cases}
\tag{14}
$$

373 Here, $\alpha_{i,j,k}$ [dm^2/s] is the water exchange coefficient in the ijk-th KHRU, $\left(h_n - h_{i,j,k}\right)$

374 [dm] is the water head difference between the rapid and slow flows at the junction of large

375 and small fissures in KHRUs, *np* is the number of fissure systems connected to the adjacent

376 conduit systems, $(K_w)_{i,j,k}$ [dm/s] is the permeability coefficient at the junction of a fissure

377 and conduit, d_{ip} and r_{ip} [dm] are the conduit diameter and radius, respectively, Δl_{ip}

378 [dm] is the length of the connection between conduits i and p, and τ_{ip} is the conduit

379 curvature. Some of the parameters in this equation, such as $(K_w)_{i,j,k}$ and $(h_n - h_{i,j,k})$,

380 were obtained by conducting an infiltration test in the study area.

381 The confluence of the underground river system plays an important role for the

382 confluence at the basin outlet. To facilitate the calculation of confluence in the QMG model,

383 the underground river systems can be generalized into large multiple conduit systems.

384 During floods, these conduit systems are mostly under pressure. Whether the water flow is

385 laminar or turbulent depends on the flow regime at that time. The water flow into these

386 conduits is calculated by the Hagen–Poiseuille equation and the Darcy–Weisbach equation

387 (Shoemaker et al., 2008):

388
$$\begin{cases} Q_{\text{laminar}} = -A\dfrac{gd^2\partial h}{32v\partial x} = -A\dfrac{\rho gd^2\Delta h}{32\mu\tau\Delta l} \\ \\ Q_{\text{turbulent}} = -2A\sqrt{\dfrac{2gd\,|\Delta h|}{\Delta l\tau}}\log\left(\dfrac{H_c}{3.71d} + \dfrac{2.51v}{d\sqrt{\dfrac{2gd^3\,|\Delta h|}{\Delta l\tau}}}\right)\dfrac{\Delta h}{|\Delta h|} \end{cases} \tag{15}$$

389 Here, Q_{laminar} [L/s] is the water flow of the laminar flow in the conduit systems, A [dm^2] is

390 the conduit cross-sectional area, d [dm] is the conduit diameter, ρ [kg/dm^3] is the density

391 of the underground river, $v=\mu/\rho$ is the coefficient of kinematic viscosity, $\Delta h/\tau\Delta l$ is

392 the hydraulic slope of the conduits, τ is the dimensionless conduit curvature, $Q_{\text{turbulent}}$ [L/s]

393 is the turbulent flow in the conduit systems and H_c [dm] is the average conduit wall height.

394 **3.2 Parameter optimization**

395 In total, the QMG model has 12 parameters, of which flow direction and slope are

396 topographic parameters that can be determined from the DEM without parametric

397 optimization, while the remaining 10 parameters require calibration. Other distributed

398 hydrological models with multiple structures usually have many parameters. For example,

399 the Karst–Liuxihe model (Li et al., 2021) has 15 parameters that must be calibrated. In the

400 QMG model, each parameter is normalized as

$$x_i = x^*_i / x_{i0}, \tag{16}$$

402 where x_i is the dimensionless parameter value i after it is normalized, x^*_i is the parameter

403 value i in actual physical units, and x_{i0} is the initial or final value of x_i. Through the

404 processing of Eq. (16), the value range of the model parameters is limited to a hypercube

405 $K_n = (X \mid 0 \leq x_i \leq 1, \ i = 1, 2, ..., n)$, K is a dimensionless value. This normalized treatment

406 ignores the influence of the spatiotemporal variation of the underlying surface attributes on

407 the parameters, while also simplifying the classification and number of the model parameters

408 to a certain extent. Accordingly, the model parameters can be divided further into

409 rainfall-evaporation ones, epikarst-zone ones and underground-river ones. Table 1 lists the

410 parameters of the QMG model.

411 **Table 1.** Parameters of QMG model.

412 Because the QMG model has relatively few parameters, it is possible to calibrate them

413 manually, which has the advantage that the operation is easy to implement and does not

414 require a special program for parameter optimization. However, the disadvantage is that it is

415 subjective, which can lead to great uncertainty in the manual parameter calibration process.

416 To compare the effects of parameter optimization on model performance, this study used

417 both manual parameter calibration and the improved chaotic particle swarm optimization

418 algorithm (IPSO) for the automatic calibration of model parameters, and compared the

419 effects of both on flood simulation.

420 In general, the structure and parameters of a standard particle swarm optimization

421 algorithm (PSO) are simple, with the initial parameter values obtained at random. For

422 parameter optimization in high-dimensional multi-peak hydrological models, the standard

423 PSO is easily limited to a local convergence and cannot achieve the optimal effect, while the

424 late evolution of the algorithm may also cause problems, such as precocity and stagnant

425 evolution, due to the 'inert' aggregation of particles, which seriously affects the efficiency of

426 parameter selection. It is necessary to overcome the above problems and make the algorithm

427 converge to the global optimal solution with a high probability. In parameter optimization

428 for the QMG model, we improved the standard PSO algorithm by adding chaos theory, and

429 developed the IPSO, where 10 cycles of chaotic disturbances were added to improve the

430 activity of the particles. The inverse mapping equation of the chaotic variable is

431
$$\begin{cases} X_{ij} = X_{\min} + (X_{\max} - X_{\min}) * Z_{ij} \\ Z'_{ij} = (1-\alpha)Z^* + \alpha Z_{ij} \end{cases} \tag{17}$$

432 where X_{ij} is the optimization variable for the model parameters, $(X_{\max} - X_{\min})$ is the

433 difference between its maximum and its minimum, Z_{ij} is the variable before the disturbance is

434 added and Z'_{ij} represents the chaotic variables after a disturbance is added, α is a variable

435 determined by the adaptive algorithm, $0 \leq \alpha \leq 1$, and Z^* is the chaotic variable formed when

436 the optimal particle maps to the interval [0,1]. In parameter optimization, the flowchart of the

437 IPSO is shown in Figure 4.

438 **Figure 4.** Algorithm flow chart of IPSO.

439 **3.3 Uncertainty analysis**

440 Uncertainties in hydrological model simulation results usually originate from three aspects:

441 input data, model structure and model parameters (Krzysztofowicz, 2014). In the present

442 study, the input data (e.g. rainfall, flood events and some hydrogeological data) were first

443 validated and pre-processed through observations to reduce their uncertainties.

444 Second, we simplified the structure of the QMG model to reduce the structural

445 uncertainty. As a mathematical and physical model, a hydrological model has some

446 uncertainty in flood simulation and forecasting because of the errors in system structure and

447 the algorithm (Krzysztofowicz and Kelly, 2000). The model was designed with full

448 consideration of the relationship between the amount of data required to build the model and

449 its performance for flood simulation and forecasting in karst regions, and the model's entire

450 framework was integrated through simple structures and easy-to-implement algorithms,

451 using the concept of distributed hydrological modelling. Conventionally, the extent of

452 uncertainty is increased with the growing complexity of the model structure. We therefore

453 ensured that the structure of the QMG model was simple when it was designed, and the

454 model was divided into surface and underground double-layer structures to reduce its

455 structural uncertainty.

456 Third, we focus on analysing the uncertainty and sensitivity of the model parameters

457 and their optimization method, for which a multi-parametric sensitivity analysis method

458 (Choi et al., 1999; Li et al., 2020) was used to analyse the sensitivity of the parameters in the

459 QMG model. The steps in the parameter sensitivity analysis are as follows.

460 1) Selection of appropriate objective function

461 The Nash–Sutcliffe coefficient is widely used as the objective function to evaluate the

462 performance of hydrological models (Li et al., 2020, 2021). It was therefore used to assess

463 the QMG model. Because the most important factor in flood forecasting is the peak

464 discharge, it is used in the Nash coefficient equation:

$$465 \qquad NSC = 1 - \frac{\sum_{i=1}^{n}\left(Q_i - Q_i^{'}\right)^2}{\sum_{i=1}^{n}\left(Q_i - \overline{Q}\right)^2}, \qquad (18)$$

466 where NSC is the Nash–Sutcliffe coefficient, Q_i [L/s] are the observed flow discharges, Q_i'

467 [L/s] are the simulated discharges, $\overline{Q}$ [L/s] is the average observed discharge and n [h] is

468 the observation period.

469 2) Parameter sequence sampling

470 The Monte Carlo sampling method was used to sample 8000 groups of parameter

471 sequences. The parametric sensitivity of the QMG model was analysed and evaluated by

472 comparing the differences between the a priori and a posteriori distributions of the

473 parameters.

474 3) Parameter sensitivity assessment

475   The a priori distribution of a model parameter means its probability distribution, while

476 the a posteriori distribution refers to the conditional distribution calculated after sample

477 sampling, and it can be calculated based on the simulation result of the parametric

478 optimization. If there is a significant difference between the priori distribution and its

479 posteriori distributionof the parameter, then the parameter being tested has a high sensitivity,

480 whereas if there is no obvious difference, then the parameter is insensitive. The parametric

481 priori distribution is calculated as

482
$$
\begin{cases}
P_{i,j}(NSC_{i,j} \geq 0.85) = \dfrac{n}{N+1} \times 100 \\
\sigma_i = \sum_{j=1}^{n} \left(P_{i,j} - \overline{P_{i,j}} \right)^2
\end{cases}
\tag{19}
$$

483 where $P_{i,j}$ is the a priori distribution's probability when $NSC_{i,j} \geq 0.85$. We used a

484 simulated Nash coefficient of 0.85 as the threshold value, and n was the number of

485 occurrences of a Nash coefficient greater than 0.85 in flood simulations. In each simulation,

486 only a certain parameter was changed, while the remaining parameters remained unchanged.

487 If the Nash coefficient of this simulation exceeded 0.85, then the flood simulation results

488 were considered acceptable. The term σ_i is the difference between the acceptable value

489 and its mean, which represents the parametric sensitivity ($0 < \sigma_i < 1$). The higher the σ_i

490 value, the more sensitive the parameter. N is the 8000 parameter sequences, and $\overline{P_{i,j}}$ is the

491 average value of the a priori distribution.

492 **3.4 Model Setting**

493   Once the model was built, some of the initial conditions had to be set before running it

494 to simulate and forecast floods, such as basin division, the setting of initial soil moisture, and

495 the assumption of the initial parameter range. 1) In the study area, the entire Qingmuguan

496 karst basin was divided into 893 KHRUs, including 65 surface river units, 466 hill slope

497 units, and 362 underground river units. The division of these units formed the basis for

498 calculating the process of runoff generation and convergence. 2) The initial soil moisture

499   was set to 0–100% of the saturation moisture content in the basin, and the specific soil

500   moisture before each flood had to be determined by a trial calculation. 3) The waterhead

501   boundary conditions of the groundwater were determined by a tracer test in the basin, where

502   a perennial stable water level adjacent the groundwater-divide was used as the fixed

503   waterhead boundary. The base flow of the underground river was determined to be 35 L/s

504   from the perennial average dry season runoff. 4) The range of initial parameters and

505   convergence conditions were assumed before parameter optimization (Figure 4). 5)

506   Parameter optimization and flood simulation validated the performance of the QMG model

507   in karst basins.

508   **4 Results and discussion**

509   **4.1 Parameter Sensitivity Results**

510   The number of parameters in a distributed hydrological model is generally large, and it

511   is important to perform a sensitivity analysis of each parameter to quantitatively assess the

512   impact of the different parameters on model performance. In the QMG model, each

513   parameter was divided into four categories according to its sensitivity: (i) highly sensitive,

514   (ii) sensitive, (iii) moderately sensitive, and (v) insensitive. In the calibration of model

515   parameters, insensitive ones do not need to be calibrated, which can greatly reduce the

516   amount of calculation and improve the efficiency of model operation.

517   The flow process in the calibration period (14 April to 10 May 2017) was adopted to

518   calculate the sensitivity of the model parameters, for which the calculation principle was

519   equation (19), and the parameter sensitivity results are calculated in Table 2.

520   Table 2 Parametric sensitivity results in QMG model.

521   In Table 2, the value of σ_i [equation (19)] represents a parameter's sensitivity, and the

522   higher the value, the more sensitive the parameter is. From the results in Table 2, it was

523   found that the rainfall infiltration coefficient, rock permeability coefficient, rock porosity,

524   and the related parameters of soil water content, such as the saturated water content, and

525   field capacity, were sensitive parameters. The order of parameter sensitivity was as follows:

526   infiltration coefficient > permeability coefficient > rock porosity > specific yield > saturated

527 water content > field capacity > flow direction > thickness > slope > Soil coefficient >

528 channel roughness > evaporation coefficient.

529   In the QMG model, parameters are classified as highly sensitive, sensitive, moderately

530 sensitive, and insensitive according to their influence on the flood simulation results. In

531 Table 4, we divided the sensitivity of model parameters into four levels based on the σ_i

532 value: 1) highly sensitive parameters, $0.8 < \sigma_i < 1$; 2) sensitive parameters, $0.65 < \sigma_i < 0.8$;

533 3) moderately sensitive parameters, $0.45 < \sigma_i < 0.65$; and 4) insensitive parameters,

534 $0 < \sigma_i < 0.45$. The highly sensitive parameters were the infiltration coefficient, permeability

535 coefficient, rock porosity, and specific yield. The sensitive parameters were the saturated

536 water content, field capacity, and thickness of the epikarst zone. The moderately sensitive

537 parameters were flow direction, slope, and soil coefficient. The insensitive parameters were

538 channel roughness and the evaporation coefficient.

539 **4.2 Parametric Optimization**

540   In total, the QMG model has 12 parameters, of which only eight need to be optimized,

541 which is relatively few for distributed models. The parameters of flow direction and slope as

542 well as the insensitive parameters of channel roughness and the evaporation coefficient need

543 not be calibrated, which can improve the convergence efficiency of the model parameter

544 optimization.

545   In the study area, 18 karst floods during the period 14 April 2017 to 10 June 2019 were

546 recorded at the underground river outlet to validate the effects of the QMG model in karst

547 hydrological simulations. The calibration period was 14 April to 10 May 2017 at the

548 beginning of the flow process, with the remainder of the time being the validation period. In

549 the QMG model, the IPSO algorithm was used to optimize the model parameters. To show

550 the necessity of parameter optimization for the distributed hydrological model, the study

551 specifically compared the flood simulations obtained using the initial parameters of the

552 model (without parameter calibration) and the optimized parameters. Figure 5 shows the

553 iteration process of parameter optimization for the QMG model.

554   Figure 5 Iteration process of parametric optimization.

555   Figure 5 shows that almost all parameters fluctuated widely at the beginning of the

556   optimization, and then after about 15 iterations of the optimization calculation, most of the

557   linear fluctuations become significantly less volatile, which indicated that the algorithm

558   tended to converge (possibly only locally). When the number of iterations exceeded 25, all

559   parameters remained essentially unchanged, meaning that the algorithm had converged (at

560   this point there was global convergence). It took only 25 iterations to reach a definite

561   convergence of the parameter rates with this IPSO algorithm, which is extremely efficient in

562   terms of the parameter optimization of distributed hydrological models. In previous studies

563   of the parametric optimization for the Karst-Liuxihe model in similar basin areas, 50

564   automatic parameter optimization iterations were required to reach convergence (Li et al.,

565   2021), demonstrating the effectiveness of the IPSO algorithm.

566   To evaluate the effect of parameter optimization, the convergence efficiency of the

567   algorithm, and more importantly, the parameters after calibration were used to simulate

568   floods. Figure 6 shows the flood simulation effects.

569   Figure 6 Flow simulation results of QMG model based on parameter optimization.

570   Figure 6 shows that the flows simulated by parameter optimization were better than

571   those simulated by the initial model parameters. The simulated flow processes based on the

572   initial parameters were relatively small, with the simulated peak flows in particular being

573   smaller than the observed values, and there were large errors between the two values. In

574   contrast, the simulated flows produced by the QMG model after parameter optimization

575   were very similar to the observed values, which indicates that calibration of the model

576   parameters is necessary and that there was an improvement in parameter optimization

577   through the use of the IPSO algorithm in this study. In addition, it was found that the flow

578   simulation effect was better in the calibration periods than in the validation periods (Fig. 6).

579   To compare the results of the flow processes simulation with the initial model

580   parameters and the optimized parameters, six evaluation indices (Nash–Sutcliffe coefficient,

581   correlation coefficient, relative flow process error, flood peak error, water balance

582   coefficient, and peak time error) were applied in this study, and the results are presented in

583   Table 3.

584   Table 3 Flood simulation evaluation index through parametric optimization.

585   Table 3 shows that the evaluation indices of the flood simulations after parametric

586   optimization were better than those of the initial model parameters. The average values of

587   the initial parameters for these six indices 0.81, 0.74, 27%, 31%, 0.80, and 5 h, respectively.

588   For the optimized parameters, the average values were 0.90, 0.91, 16%, 14%, 0.94, and 3 h,

589   respectively. The flood simulation effects after parameter optimization clearly improved,

590   implying that parameter optimization for the QMG model is necessary, and the IPSO

591   algorithm for parameter optimization is an effective approach that can greatly improve the

592   convergence efficiency of parameter optimization, and also ensure that the model performs

593   well in flood simulations.

594   **4.3 Model Validation in Flood Simulations**

595   Following parameter optimization, we simulated the whole flow process (14 April 2017

596   to 10 June 2019) based on the optimized and initial parameters of the QMG model (Fig. 6),

597   which enabled a visual reflection of the model used in the simulation of a long series of flow

598   processes. To reflect the simulation effect of the model for different flood events, we divided

599   the whole flow process into 18 flood events, then used the initial parameters of the model

600   and the optimized parameters, respectively, to verify the model performance in flood

601   simulations. Figure 7 and Table 4 show the flood simulation effects and their evaluation

602   indices using both the initial and the optimized parameters.

603   Figure 7 Flood simulation effects based on initial and optimized parameters.

604   Table 4 Flood simulation indices for model validation.

605   Figure 7 shows that the flood simulation results using the initial parameters were

606   smaller than the observed values, and the model performance improved in flood simulations

607   after parameter optimization. The simulated flood processes were in good agreement with

608   observations, and were especially effective for simulating flood peak flows. From flood

609   simulation indices in Table 4, the average water balance coefficient based on the initial

parameters was 0.69, i.e., much less than 1, indicating that the simulated water in the model was unbalanced. After parameter optimization, the average value was 0.92, indicating that parameter optimization had a significant impact on the model water balance calculation.

Table 4 shows that the average values of the six indices (Nash–Sutcliffe coefficient, correlation coefficient, relative flow process error, flood peak error, water balance coefficient, and peak time error) for the initial parameters were 0.79, 0.74, 26%, 25%, 0.69, and 5 h, respectively, while for the optimized parameters the average values were 0.92, 0.90, 10%, 11%, 0.92, and 2 h, respectively. All evaluation indices improved after parameter optimization, with the average values of the Nash coefficient, correlation coefficient, and water balance coefficient increasing by 0.13, 0.16, and 0.23, respectively. The average values of the relative flow process error, flood peak error, and peak time error decreased by 15%, 14%, and 3 h, respectively. These reasonable flood simulation results confirmed that parameter optimization by the IPSO algorithm was necessary and effective for the QMG model.

Compared with the overall flow process simulation shown in Figure 6, each flood process was better simulated by the QMG model (Fig. 7). This was because in the function of the QMG model and its algorithm design, the main consideration was the calculation of the flood process, but the correlation algorithm of the dry season runoff was not described well enough. For example, equations (12)–(15) are the flood convergence algorithm. As a result, the model is not good at simulating other flow processes, such as dry season runoff, leading to a low accuracy in the overall flow process. The next phase of our research will focus on refining the algorithm related to dry season runoff and improving the comprehensive performance of the model.

4.4 Uncertainty analysis

4.4.1 Assessment and reduction of uncertainty

In general, the uncertainty in model simulation is due mainly to three aspects of the model: (i) the uncertainty of its input data, (ii) the uncertainty of its structure and algorithm and (iii) the uncertainty of its parameters. In the practical application of a hydrological model, these

three uncertainties are usually interwoven, which leads to the overall uncertainty of the final

simulation results (Krzysztofowicz, 2014). Therefore, the present study focused on the

uncertainties in the input data, the model structure and the parameters to reduce the overall

uncertainty of the simulation results.

First, the input data—mainly rainfall-runoff data and hydrogeological data—were

pre-processed, which substantially reduced their uncertainty. Second, we simplified the

structure of the QMG model, which is reflected in the fact that it has only two layers of

spatial structure in the horizontal and vertical directions. This relatively simple structure

reduced greatly the uncertainty due to the model structure. In contrast, the underground

structure of our previous Karst–Liuxihe model (Li et al., 2021) has five layers, which leads

to great uncertainty. Third, appropriate algorithms for runoff generation and confluence were

selected. Different models were designed for different purposes, which leads to great

differences in the algorithms used. In the QMG model, most of the rainfall-runoff algorithms

used have been validated by the research results of others, and some of them were improved

to suit karst flood simulation and forecasting by the QMG model. For example, the

algorithm for the generation of excess infiltration runoff [Eq. (2)] was an improvement of

the version used in the Liuxihe model (Chen, 2009, 2018; Li et al., 2020). Finally, the

algorithm for parameter optimization was improved. Considering the shortcomings of the

standard PSO algorithm that tends to converge locally, this study developed the IPSO for

parameter optimization by adding chaotic perturbation factors. The flood simulation results

after parameter optimization were much better than those of the initial model parameters

(Figs. 6 and 7 and Tables 2 and 3), which indicates that parameter optimization is necessary

for a distributed hydrological model and can reduce the uncertainty of the model parameters.

4.4.2 Parameter sensitivity analysis

The parameter-sensitivity results in Table 2 show that the rainfall-infiltration coefficient in

the QMG model was the most sensitive parameter. It was the key to determining the

generation of excess infiltration surface runoff and separating surface runoff from subsurface

runoff. If the rainfall infiltration coefficient was greater than the infiltration capacity, excess

infiltration surface runoff was generated on the exposed karst landforms; otherwise, all

667 rainfall would infiltrate to meet the water deficit in the vadose zone, and then continue to

668 seep down into the underground river system, eventually flowing out of the basin through

669 the underground river outlet. The confluence modes of surface runoff and underground

670 runoff were completely different, resulting in a large difference in the simulated flow results.

671 Therefore, the rainfall infiltration coefficient had the greatest impact on the final flood

672 simulation results.

673 Other highly sensitive parameters such as the rock permeability coefficient, rock

674 porosity and specific yield were used as the basis for dividing between slow flow in karst

675 fissures and rapid flow in conduits. The division of slow and rapid flows also had a great

676 impact on the discharge at the outlet of the basin. Slow flow plays an important role in water

677 storage in a karst aquifer and is very important for the replenishment of river base flow in

678 the dry season. Rapid flow in large conduit systems dominates the flood runoff and is the

679 main component of the flood water volume in the flood season.

680 Parameters related to the soil water content, including the saturated water content, field

681 capacity and thickness, were sensitive parameters and had a large influence on the flood

682 simulation results. This is because the soil moisture content prior to flooding affects how

683 flood flows rise and when peaks occur. If the soil is already very wet or even saturated

684 before the flooding, the flood will rise quickly to reach a peak, and the process line of the

685 flood peak flow will be sharp and thin. This type of flood process forms easily and can lead

686 to disaster-causing flood events. In contrast, if the soil in the basin is very dry before the

687 flooding, the rainfall will first meet the water shortage of the vadose zone, and after it is

688 replenished the rainfall will infiltrate into the underground river. The flood peak of the river

689 basin outlet is therefore delayed.

690 The moderately sensitive parameters were flow direction, slope and the soil coefficient.

691 They had a specific influence on the flood simulation results, but the influence was not as

692 great as that of the highly sensitive and sensitive parameters. The insensitive parameters

693 were channel roughness and the evaporation coefficient. The amount of water lost by

694 evapotranspiration is very small in the total flood water, and it was therefore the least

695 sensitive parameter in the QMG model.

5 Conclusions

This study proposed a new distributed physically based hydrological model, i.e. the QMG model, to simulate floods accurately in karst trough and valley landforms. The main conclusions of this paper are as follows.

This QMG model has a high application potential in karst hydrology simulations. Other distributed hydrological models usually have multiple structures, resulting in the need for a large amount of data to build models in karst areas (Kraller et al., 2014). The QMG model has only a double-layer structure, with a clear physical meaning, and a small amount of basic data is needed to build the model in karst areas, such as some necessary hydrogeological data. For example, the distribution and flow direction of underground rivers is required, which can be inferred from a tracer test, leading to a low modelling cost. There were fewer parameters in the QMG model than in other distributed hydrological models, with only 10 parameters that needed to be calibrated.

The flood simulation after parameter optimization was much better than the simulation using the initial model parameters. After parameter optimization, the average values of the Nash coefficient, correlation coefficient and water balance coefficient increased by 0.13, 0.16 and 0.23, respectively, while the average relative flow process error, flood peak error and peak time error decreased by 15%, 14% and 3 h, respectively. Parameter optimization is necessary for a distributed hydrological model, and the improvement of the IPSO algorithm in this study was an effective way to achieve this.

In the QMG model, the rainfall infiltration coefficient I_c, rock permeability coefficient K, rock porosity R_p and the parameters related to the soil water content were sensitive parameters. The order of parameter sensitivity was infiltration coefficient > permeability coefficient > rock porosity > specific yield > saturated water content > field capacity > flow direction > thickness > slope > soil coefficient > channel roughness > evaporation coefficient.

This QMG model is suitable for karst trough and valley landform like this study area, where the topography is conducive to the spread of flood water. Whether this model is

applicable to the karst areas of other landforms still needs to be verified in the future studies.

In addition, the basin area is very small, where the hydrological similarity between different

small basin areas varies greatly (Kong and Rui, 2003). The size of the area to be modelled

has a great influence on the choice of model spatial resolution (Chen et al., 2017). Therefore,

whether the QMG model is suitable for flood forecasting in large karst basins needs to be

determined.

Model development.

This QMG model presented in this study uses the Visual Basic language programming. The
general framework of the model and the algorithm consist of three parts: the modeling
approach, the algorithm of rainfall-runoff generation and confluence, and the parameter
optimization algorithm. As a free and open source hydrological modeling program (QMG
model-V1.0), we provide all modeling packages, including model code, installation package,
simulation data package and user manual, free of charge. It is important to note that the
model we provide are for scientific research purposes only and should not be used for any
commercial purposes. Creative Commons Attribution 4.0 International.
Model installation program can be downloaded from ZENODO, cite as JI LI. (2021, June
16). QMG model-V1.0. Zenodo. http://doi.org/10.5281/zenodo.4964701, and
http://doi.org/10.5281/zenodo.4964697 (registration required). User manual can be
downloaded from http://doi.org/10.5281/zenodo.4964754.

Code availability.

All code for the QMG model-V1.0 in this paper are available and free, the code can be
downloaded from ZENODO, Cite as JI LI. (2021, June 16). QMG model-V1.0 code
(Version v1.0). Zenodo. http://doi.org/10.5281/zenodo.4964709 (registration required).

Data availability.

All data used in this paper are available, findable, accessible, interoperable, and reusable.
The simulation data and modelling data package can be downloaded from
http://doi.org/10.5281/zenodo.4964727. The DEM was downloaded from the Shuttle Radar
Topography Mission database at http://srtm.csi.cgiar.org. The land use-type data were
downloaded from http://landcover.usgs.gov, and the soil-type data were downloaded from
http://www.isric.org. These data were last accessed on 15 October 2020.

Author contributions. JIL was responsible for the calculations and writing of the whole

paper. DY helped conceive the structure of the model. ZF and JL provided significant

assistance in the English translation of the paper. MM provided flow data of the study area.

757 **Competing interests.**

758 The authors declare that they have no conflicts of interest.

759 **Acknowledgments.**

760 This study was supported by the National Natural Science Foundation of China (41830648),

761 the National Science Foundation for Young Scientists of China (42101031), Fundamental

762 Research Funds for the Central Universities (), Chongqing Natural Science Foundation

763 (cstc2021jcyj-msxm0007), the Chongqing Education Commission Science and technology

764 research Foundation (KJQN202100201), the drought monitoring, analysising and early

765 warning of typical prone-to-drought areas of Chongqing (20C00183), and the Open Project

766 Program of Guangxi Key Science and Technology Innovation Base on Karst Dynamics

767 (KDL & Guangxi 202009, KDL & Guangxi 202012).

References

Abbott, M. B., Bathurst, J. C., Cunge, J. A., O'Connell, P. E., and Rasmussen, J.: An Introduction to the European HydrologicSystem-System Hydrologue Europeen, 'SHE', a: History and Philosophy of a Physically-based, Distributed Modelling System,J. Hydrol., 87, 45–59, 1986a.

Abbott, M. B., Bathurst, J. C., Cunge, J. A., O'Connell, P. E., and Rasmussen, J.: An Introduction to the European Hydrologic System-System Hydrologue Europeen, 'SHE', b: Structure of a Physically based, distributed modeling System, J. Hydrol., 87,61–77, 1986b.

Ambroise, B., Beven, K., and Freer, J.: Toward a generalization of the TOPMODEL concepts: Topographic indices of hydrologic similarity. Water Resources Research, 32, 2135-2145, 1996.

Atkinson, T.C.: Diffuse flow and conduit flow in limestone terrain in the Mendip Hills, Somerset (Great Britain). Journal of Hydrology, 35, 93-110. https://doi.org/10.1016/0022-1694(77)90079-8, 1977.

Berry, R.A., Saurel, R., and Lemetayer, O.: The discrete equation method (DEM) for fully compressible, two-phase flows in ducts of spatially varying cross-section. Nuclear Engineering & Design, 240(11), 3797-3818, 2010.

Beven, K., and Binley, A.: The future of distributed models: Model calibration and uncertainty prediction. Hydrological Processes, 6, 279-298, 2006.

Birk, S., Geyer, T., Liedl, R., and Sauter, M.: Process-based interpretation of tracer tests in carbonate aquifers. Ground Water, 43(3), 381-388, 2005.

Bittner, D., Parente, M.T., Mattis, S., Wohlmuth, B., and Chiogna, G.: Identifying relevant hydrological and catchment properties in active subspaces: An inference study of a lumped karst aquifer model. ADVANCES IN WATER RESOURCES,135,550-560.

doi: 10.1016/j.advwatres.2019.103472, 2020.

794   Blansett, K. L., and Hamlett, J. M.: Challenges of Stormwater Modeling for Urbanized Karst

795   Basins. Pittsburgh, Pennsylvania, an ASABE Meeting Presentation, Paper Number:

796   1009274. doi:10.13031/2013.29840, 2010.

797   Blansett, K. L.: Flow, water quality, and SWMM model analysis for five urban karst basins..

798   (Doctoral dissertation). The Pennsylvania State University,USA, 2011.

799   Bonacci, O., Ljubenkov, I., and Roje-Bonacci, T.: Karst flash floods: an example from

800   the Dinaric karst Croatia. Nat. Hazards Earth Syst. Sci. 6, 195–203, 2006.

801   Chang, Y., and Liu, L.: A review of hydrological models in karst areas. Engineering

802   investigation, 43,37-44, 2015.

803   Chen, G.M., Jia, J.Y., and Han, Q.: Research on inertia weight reduction strategy of Particle

804   Swarm optimization algorithm. Journal of Xi'an Jiaotong University, 40(1),53-56, 2006.

805   Choi, J., Harvey, J. W., and Conklin, M. H.: Use of multi-parameter sensitivity analysis to

806   determine relative importance of factors influencing natural attenuation of mining

807   contaminants. the Toxic Substances Hydrology Program Meeting, Charleston,South

808   Carolina, 1999.

809   Chen, Y. B.: Liuxihe Model, China Science and Technology Press, Beijing, China, 2009.

810   Chen, Y., Li, J., and Xu, H.: Improving flood forecasting capability of physically based

811   distributed hydrological models by parameter optimization. Hydrol. Earth Syst. Sci. 20,

812   375-392. https://doi.org/10.5194/hess-20-375-2016, 2016.

813   Chen, Y., Li, J., Wang, H., Qin, J., and Dong, L.: Large watershed flood forecasting with

814   high-resolution distributed hydrological model. Hydrol. Earth Syst. Sci. 21, 735-749.

815   https://doi.org/10.5194/hess-21-735-2017, 2017.

816   Chen, Y.: Distributed Hydrological Models. Springer Berlin Heidelberg, Berlin, Germany.

817   https://doi.org/10.1007/978-3-642-40457-3_23-1, 2018.

818   Dewandel, B., Lachassagne, P., Bakalowicz, M., Weng, P., and Malki, A.A.: Evaluation of

819   aquifer thickness by analysing recession hydrographs. Application to the Oman

820   ophiolite hard-rock aquifer. Journal of Hydrology, 274,248-269, 2003.

821 Dubois, E., Doummar, J., Séverin Pistre, S., and Larocque, M.: Calibration of a lumped karst
822   system model and application to the Qachqouch karst spring (Lebanon) under climate
823   change conditions. Hydrol. Earth Syst. Sci., 24, 4275-4290.
824   https://doi.org/10.5194/hess-24-4275-2020, 2020.

825 Doummar, J., Sauter, M., and Geyer, T.: Simulation of flow processes in a large scale karst
826   system with an integrated catchment model (MIKE SHE) – identification of relevant
827   parameters influencing spring discharge. Journal of Hydrology, 426-427, 112-123,
828   2012.

829 Epting, J., Page, R.M., and Auckenthaler, A.: Process-based monitoring and modeling of
830   Karst springs–Linking intrinsic to specific vulnerability. Science of the Total
831   Environment, 625, 403-415, 2018.

832 Fleury, P., Plagnes, V., and Bakalowicz, M.: Modelling of the functioning of karst aquifers
833   with a reservoir model: Application to Fontaine de Vaucluse (South of France). Journal
834   of Hydrology, 345,38-49. http://dx.doi.org/10.1016/j.jhydrol.2007.07.014, 2007b.

835 Ford, D. C., and Williams, P.W.: Karst geomorphology and hydrology. Wiley, Chichester,
836   England, 2007.

837 Gang, L., Tong, F.G., and Bin,T.: A Finite Element Model for Simulating Surface Runoff and
838   Unsaturated Seepage Flow in the Shallow Subsurface. Hydrological Processes,
839   6,102-120. doi: 10.1002/hyp.13564, 2019.

840 Geyer, T., Birk, S., Liedl, R., and Sauter, M.: Quantification of temporal distribution of
841   recharge in karst systems from spring hydrographs. Journal of Hydrology, 348(30),
842   452-463, 2008.

843 Gou, P.F., Jiang, Y.J., Hu, Z.Y., Pu, J.B., and Yang, P.H.: A study of the variations in
844   hydrology and hydrochemistry under the condition of a storm in a typical karst
845   subterranean stream. HYDROGEOLOGY&ENGINEERING GEOLOGY,37(5),20-25,
846   2010.

847   Gutierrez, F.: Hazards associated with karst. In: Alcantara, I. & A. Goudie (Eds.),

848   Geomorphological Hazards and Disaster Prevention. Cambridge University Press,

849   Cambridge, 161–175, 2010.

850   Gutierrez, F., Parise, M., D' Waele, J., and Jourde, H.:   A review on natural and human-

851   induced geohazards and impacts in karst. Earth Science Reviews, 138, 61-88, 2014.

852   Hartmann, A., and Baker, A.: Progress in the hydrologic simulation of time variant of karst

853   systems-Exemplified at a karst spring in Southern Spain. Advances in Water Resources,

854   54,149-160, 2013.

855   Hartmann, A., Goldscheider, N., Wagener, T., Lange, J., and Weiler, M.: Karst water

856   resources in a changing world: Review of hydrological modeling approaches. Reviews

857   of Geophysics 52: 218-242. doi: 10.1002/2013RG000443, 2014a.

858   Hartmann, A., and Baker, A.: Modelling karst vadose zone hydrology and its relevance for

859   paleoclimate reconstruction. Earth-Science Reviews, 172, 178-192, 2017.

860   Hartmann, A.: Experiences in calibrating and evaluating lumped karst hydrological models.

861   London: Geological Society, Special Publications, 2018.

862   Jourde, H., Roesch, A., Guinot, V., and Bailly-Comte, V.: Dynamics and contribution of

863   karst groundwater to surface flow during Mediterranean flood. Environ. Geol. 51 (5),

864   725–730, 2007.

865   Jourde, H., Lafare, A., Mazzilli, N., Belaud, G., Neppel, L., Doerfliger, N., and Cernesson, F.:

866   Flash flood mitigation as a positive consequence of anthropogenic forcings on the

867   groundwater resource in a karst catchment. Environ. Earth Sci. 71, 573–583,2014.

868   Jukić, D., and Denić-Jukić, V.: Groundwater balance estimation in karst by using a

869   conceptual rainfall–runoff model. Journal of Hydrology, 373, 302-315.

870   http://dx.doi.org/10.1016/j.jhydrol.2009.04.035, 2009.

871   Kong, F.Z., and Rui, X.F.: Hydrological similarity of catchments based on topography.

GEOGRAPHICAL RESEARCH, (06), 709-715, 2003.

Kovács, A., and Sauter, M.: Modelling karst hydrodynamics. In: Goldscheider N, Drew D (eds) Methods in karst hydrogeology, IAH international contributions to hydrogeology; 26,264 p, 2007.

Kovács, A., and Perrochet, P.: A quantitative approach to spring hydrograph decomposition. Journal of Hydrology, 352, 16-29. http://dx.doi.org/10.1016/j.jhydrol.2007.12.009, 2008.

Kurtulus, B., and Razack, M.: Evaluation of the ability of an artificial neural network model to simulate the input-output responses of a large karstic aquifer: the la rochefoucauld aquifer (charente, france). Hydrogeology Journal, 15(2), 241-254, 2007.

Krzysztofowicz, R., and Kelly, K.: Hydrologic uncertainty processor for probabilistic river stage forecasting. Water Resources Research, 36(11),3265-3277, 2000.

Krzysztofowicz, R.: Probabilistic flood forecast: Exact and approximate predictive distributions. Journal of Hydrology, 517(1), 643-651, 2014.

Kraller, G., Warscher, M., Strasser, U., Kunstmann, H., and Franz, H.: Distributed hydrological modeling and model adaption in high alpine karst at regional scale (berchtesgaden alps, germany). Springer International Publishing Switzerland. https://doi.org/10.1007/978-3-319-06139-9_8, 2014.

Ladouche, B., Marechal, J. C., and Dorfliger, N.: Semi-distributed lumped model of a karst system under active management. Journal of Hydrology, 509,215-230, 2014.

Li, J., Chen, Y., Wang, H., Qin, J., Li, J., and Chiao, S.: Extending flood forecasting lead time in a large basin by coupling WRF QPF with a distributed hydrological model, Hydrol. Earth Syst. Sci. 21, 1279–1294. https://doi.org/10.5194/hess-21-1279-2017, 2017.

Li, J., Yuan, D., Liu, J., Jiang, Y., Chen, Y., Hsu, K. L., and Sorooshian, S.: Predicting floods in a large karst river basin by coupling PERSIANN-CCS QPEs with a physically based distributed hydrological model. Hydrol. Earth Syst. Sci. 23, 1505-1532.

899   https://doi.org/10.5194/hess-23-1505-2019, 2019.

900   Li, J., Hong, A., Yuan, D., Jiang,Y., Deng,S., Cao,C., and Liu, J.: A new distributed

901   karst-tunnel hydrological model and tunnel hydrological effect simulations. Journal of

902   Hydrology, 593, 125639. https://doi.org/10.1016/j.jhydrol.2020.125639, 2020.

903   Li, J., Hong, A., Yuan, D., Jiang,Y., Zhang,Y., Deng,S., Cao,C., Liu, J., and Chen,Y.:

904   Elaborate Simulations and Forecasting of the Effects of Urbanization on Karst Flood

905   Events   Using   the   Improved   Karst-Liuxihe   Model.CATENA,197,104990.

906   https://doi.org/10.1016/j.catena.2020.104990, 2021.

907   Liedl, R.., Sauter, M., Huckinghaus, D., Clemens, T., and Teutsch, G.: Simulation of the

908   development of karst aquifers using a coupled continuum pipe flow model. Water

909   Resources Research, 39, 50-57, 2003.

910   Liu, X., Jiang, Y.J., Ye, M.Y., Yang, P.H., Hu, Z.Y., and Li, Y.Q.: Study on hydrologic regime

911   of underground river in typical karst valley- A case study on the Qingmuguan

912   subterranean stream in Chongqing. CARSOLOGICA SINICA, 28(2),149-154, 2009.

913   Lu, D. B., Shi, Z. T., Gu, S. X., and Zeng, J. J.: Application of Hydrological Model in the

914   Karst Area. Water-saving irrigation.11, 31-34. doi:1007-4929(2013)11-031-04, 2013.

915   Martinotti, M.E., Pisano, L., Marchesini, I., Rossi, M., Peruccacci, S., Brunetti, M.T.,

916   Melillo, M.,Amoruso, G., Loiacono, P., Vennari, C., Vessia, G., Trabace, M., Parise, M.,

917   and Guzzetti, F.: Landslides, floods and sinkholes in a karst environment: the 1–6

918   September 2014 Gargano event, southern Italy. Natural Hazards and Earth System

919   Sciences, 17, 467-480, 2017.

920   Meng, H.H., Wang, N.C., Su, W.C., and Huo, Y.: Modeling and application of karst

921   semi-distributed hydrological model based on sinkholes. SCIENTIA GEOGRAPHICA

922   SINICA, 5, 550-554. doi: 10.3969/j.issn.1000-0690.2009.04.014, 2009.

923   Meng, H.H., and Wang, N.C.: Advances in the study of hydrological models in karst basin.

924   Progress in Geography, 29,1311-1318, 2010.

925   Pan, H.Y.: Hydrological model and application in karst watersheds. China University of

Geosciences. Doctoral Dissertation, Wuhan, China, 2014.

Parise, M.: Hazards in karst, Proceedings Int. Conf. "Sustainability of the karst environment. Dinaric karst and other karst regions", IHP-Unesco, Series on Groundwater,2, 155-162, 2010.

Peterson, E.W., and Wicks, C. M.: Assessing the importance of conduit geometry and physical parameters in karst systems using the storm water management model (SWMM).Journal of Hydrology, 329, 1-2, 294-305, 2006.

Peterson, J.R., and Hamlett, J.M.: Hydrologic calibration of the SWAT model in a basin containing fragipan soils. JAWRA Journal of the American Water Resources Association. doi: 10.1111/j.1752-1688.1998. tb00952.x, 1998.

Petrie, R., Denvil, S., Ames, S.,et al.: Coordinating an operational data distribution network for CMIP6 data, Geosci. Model Dev., 14, 629–644.

https://doi.org/10.5194/gmd-14-629-2021, 2021.

Qin, J.G., and Jiang, Y.P.: A review of numerical simulation methods for CFP pipeline flow. Groundwater. 3, 98-100, 2014.

Reimann, T., Melissa, E., and Hill.: Modflow-cfp: a new conduit flow process for modflow–2005. Ground Water,47(3),321-325. doi:10.1111/j.1745-6584.2009.00561.x, 2009.

Ren, Q.W.: Water Quantity Evaluation Methodology Based on Modified SWAT Hydrological Modeling in Southwest Karst Area, China University of Geoscience, Wuhan, China, 2006.

Shoemaker, W.B., Cunningham, K.J., and Kuniansky, E.L.: Effects of turbulence on hydraulic heads and parameter sensitivities in preferential groundwater flow layers. Water Resources Research, 44, 34-50. doi: 10.1029/2007WR006601, 2008.

Suo, L.T., Wan, J.W., and Lu, X.W.: Improvement and application of TOPMODEL in karst region. Carsologica Sinica, 26(1), 67-70, 2007.

952 Teixeiraparente, M., Bittner, D., Mattis, S.A., Chiogna, G , and Wohlmuth, B.:

953   Bayesian calibration and sensitivity analysis for a karst aquifer model using active

954   subspaces. Water Resources Research, 55, 342-356. doi: 10.1029/2019WR024739,

955   2019.

956 White, W.B.: Karst hydrology: recent developments and open questions. Eng. Geol. 65,

957   85–105, 2002.

958 Williams, P.W.: The role of the epikarst in karst and cave hydrogeology: a review. Int. J.

959   Speleol. 37, 1–10, 2008.

960 Williams, P. W.: Book Review: Methods in Karst Hydrogeology, Nico Goldscheider and

961   David Drew (eds). Hydrogeology Journal, 17,1025-1025, 2009.

962 Worthington, S., Ford, D., and Beddows, P.: Porosity and permeability enhancement in

963   unconfined carbonate aquifers as a result of solution. Speleogenesis: evolution of karst

964   aquifers, 2000.

965 Yang, P. H., Luo, J.Y., Peng, W., Xia, K.S., and Lin, Y.S.: Application of online technique in

966   tracer test-A case in Qingmuguan subterranean river system, Chongqing, China.

967   CARSOLOGICA SINICA, 27(3),215-220, 2008.

968 Yu, D., Yin, J., Wilby, R.L., Stuart, N. L., Jeroen, C., Lin, N., Liu, M., Yuan, H., Chen, J.,

969   Christel, P., Guan, M., Avinoam, B., Charlie, W. D., Tang, X., Yu, L., and Xu, S.:

970   Disruption of emergency response to vulnerable populations during floods. Nature

971   Sustainability, 3, 728–736. https://doi.org/10.1038/s41893-020-0516-7, 2020.

972 Yu, Q., Yang, P.H., Yu, Z.L., Chen, X.B., and Wu, H.: Dominant factors controlling

973   hydrochemical variationg of karst underground river in different period,

974   Qingmuguan,Chongqing. CARSOLOGICA SINICA, 35(2),134-143, 2016.

975 Zhang, Q.: Assesment on the intrinsic vulnerability of karst groundwater source in the

976   Qingmuguan karst valley. CARSOLOGICA SINICA, 31(1),67-73, 2012.

977 Zhu, C., and Li, Y.: Long-Term Hydrological Impacts of Land Use/Land Cover Change

978   From 1984 to 2010 in the Little River Basin, Tennessee. International Soil and Water

980 **Tables**

981 Table 1 Parameters of the QMG model.

Parameters	Variable name	Physical property
Infiltration coefficient	I_c	Meteorology
Evaporation coefficient	λ	Vegetation cover
Soil thickness	h	Karst aquifer
Soil coefficient	S_b	Soil type
Saturated water content	S_c	Soil type
Rock porosity	R_p	Karst aquifer
Field capacity	F_c	Soil type
Permeability coefficient	K	Karst aquifer
Flow direction	F_d	Landform
Slope	S_0	Landform
Specific yield	S_y	Karst aquifer
Channel roughness	n	Landform

982 Table 2 Parametric sensitivity results in QMG model.

I_c	λ	h	S_b	S_c	S_y	F_d	S_0	R_p	F_c	K	n
0.92	0.24	0.71	0.58	0.8	0.83	0.74	0.68	0.86	0.78	0.89	0.36

983 Table 3 Flood simulation evaluation index through parametric optimization.

Parameter optimization	Parameter types	Nash coefficient	Correlation coefficient	Relative flow process error/%	Flood peak error/%	Water balance coefficient	Peak time error (hours)
calibration	initial	0.82	0.77	24	29	0.82	4
periods	optimized	0.91	0.94	14	12	0.95	2
validation	initial	0.79	0.71	29	32	0.77	6
periods	optimized	0.88	0.87	18	16	0.92	3
average	initial	0.81	0.74	27	31	0.8	5
value	optimized	0.9	0.91	16	14	0.94	3

984 Table 4 Flood simulation indices for model validation.

Floods	Parameter types	Nash coefficient	Correlation coefficient	Relative flow process error/%	Flood peak error/%	Water balance coefficient	Peak time error/ (hours)
2017042408	initial	0.77	0.7	28	29	0.71	-5
	optimized	0.95	0.89	11	15	0.88	-2
2017050816	initial	0.78	0.71	19	19	0.76	-4
	optimized	0.92	0.88	11	9	0.94	-2
2017061518	initial	0.76	0.6	25	32	0.63	-5

	optimized	0.91	0.93	12	11	0.95	-3
2017071015	initial	0.78	0.82	25	37	0.64	-4
	optimized	0.92	0.87	8	7	0.94	-2
2017091512	initial	0.81	0.62	21	16	0.78	-5
	optimized	0.9	0.92	13	10	0.9	-4
2017100815	initial	0.75	0.68	30	26	0.62	-2
	optimized	0.94	0.86	11	15	0.92	-1
2018052016	initial	0.78	0.68	25	21	0.67	5
	optimized	0.91	0.93	10	13	0.94	2
2018060815	initial	0.82	0.79	27	22	0.69	-6
	optimized	0.9	0.92	11	12	0.93	-4
2018071212	initial	0.84	0.75	26	24	0.61	5
	optimized	0.91	0.88	8	15	0.92	3
2018081512	initial	0.71	0.78	26	24	0.78	-4
	optimized	0.89	0.94	12	11	0.89	-3
2018090516	initial	0.85	0.68	28	23	0.68	-5
	optimized	0.93	0.87	12	10	0.92	-2
2018092514	initial	0.79	0.78	23	19	0.59	5
	optimized	0.88	0.88	9	11	0.89	2
2018101208	initial	0.78	0.81	28	25	0.63	5
	optimized	0.92	0.94	11	10	0.94	2
2018111208	initial	0.79	0.81	25	24	0.65	-6
	optimized	0.94	0.86	13	12	0.92	-2
2019042512	initial	0.78	0.8	26	36	0.8	5
	optimized	0.89	0.94	9	16	0.93	2
2019051513	initial	0.84	0.77	32	27	0.79	4
	optimized	0.91	0.88	9	13	0.95	2
2019052516	initial	0.74	0.75	29	26	0.63	-5
	optimized	0.92	0.86	7	15	0.96	-2
2019060518	initial	0.85	0.83	28	25	0.78	-4
	optimized	0.95	0.96	10	12	0.92	-2
average value	initial	0.79	0.74	26	25	0.69	5
	optimized	0.92	0.9	10	11	0.92	2

985   **Figures**
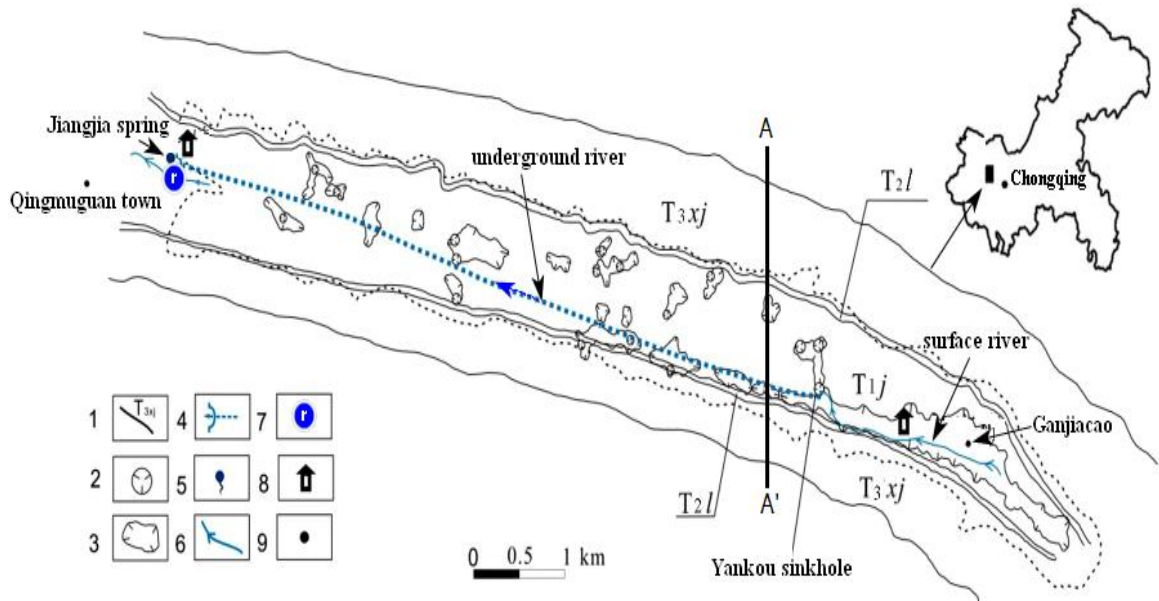
986

987   1- stratigraphic boundary, 2-sinkhole, 3- karst depression, 4- underground river, 5-
988   karst spring, 6-surface river,7-river gauge, 8- rain gauge, and 9- geographical name
989   a.   Qingmuguan karst basin (modified from Yu et al.,2016)
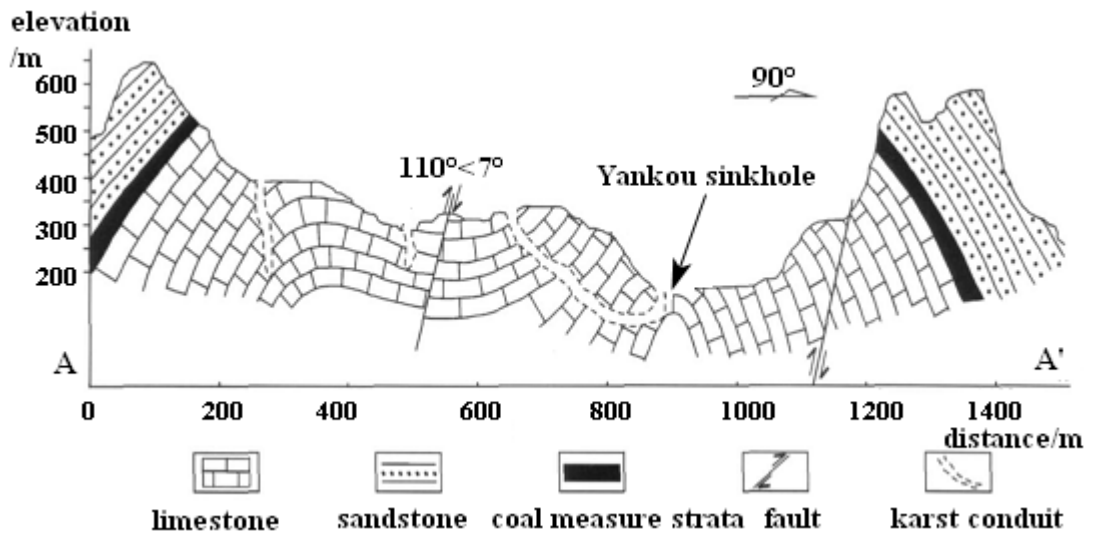
990

991   b. Lithologic cross section of Yankou sinkhole/AA'(modified from Zhang,2012)

992
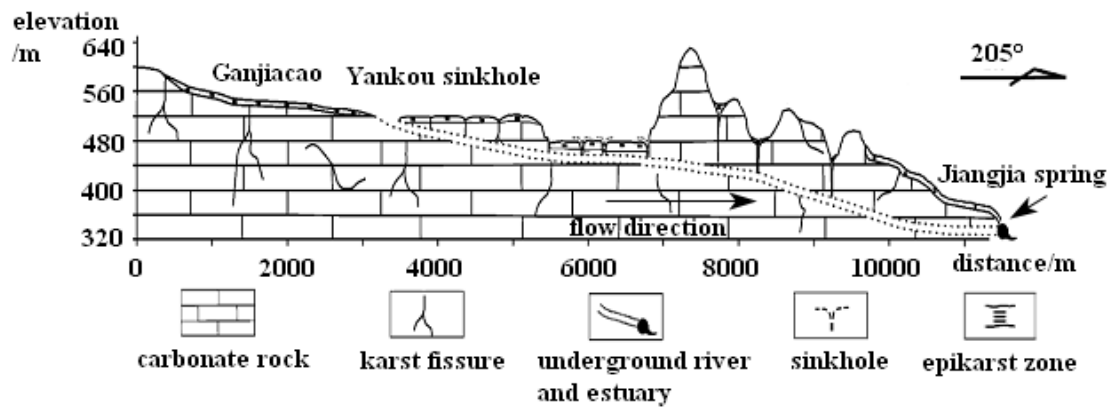
993   c. Longitudinal profile of the study area (modified from Yang et al.,2008)

994   Figure 1 The Qingmuguan karst basin.

995
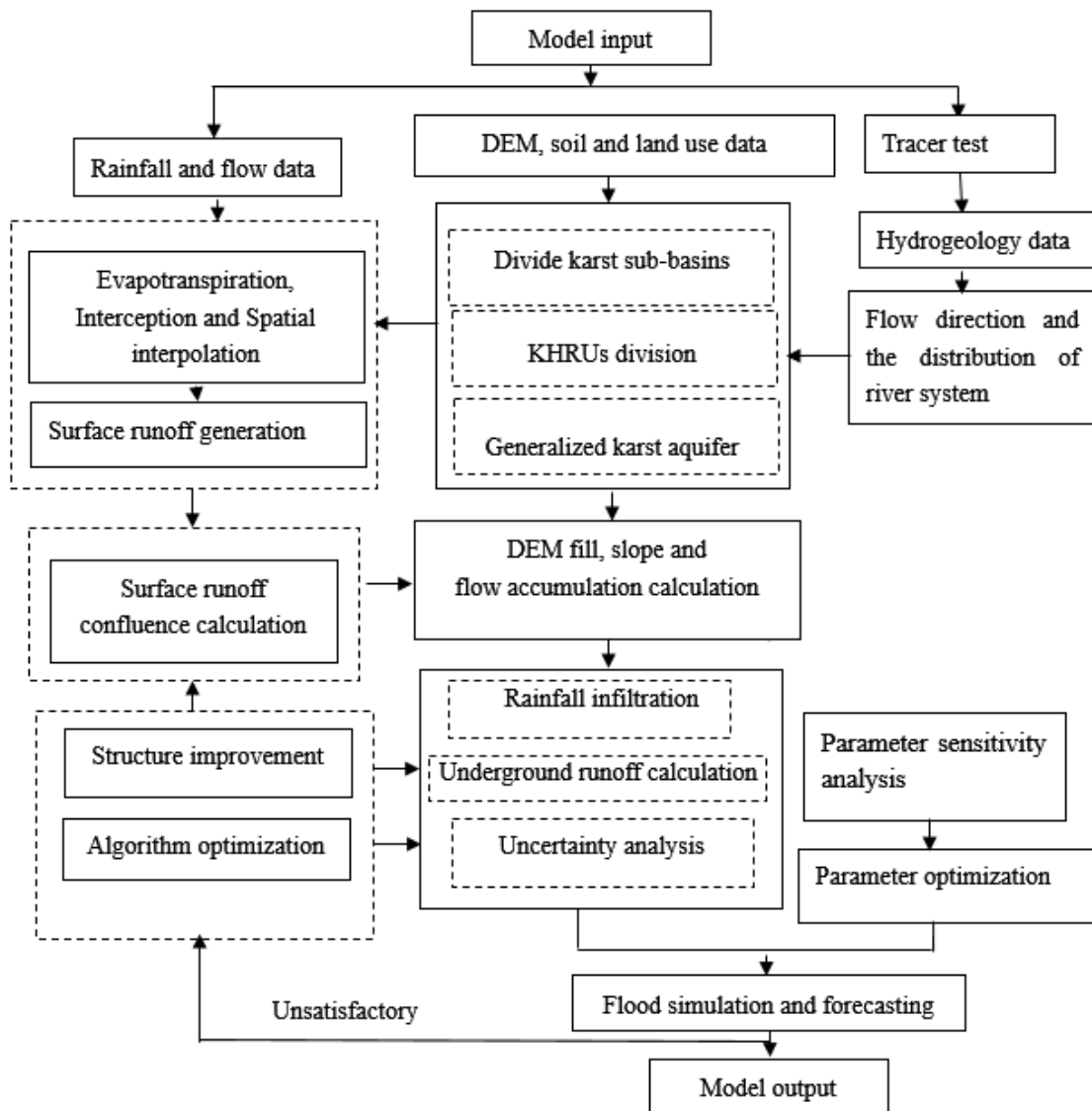
996   Figure 2 Modeling flow chart of QMG (Qingmuguan) model.
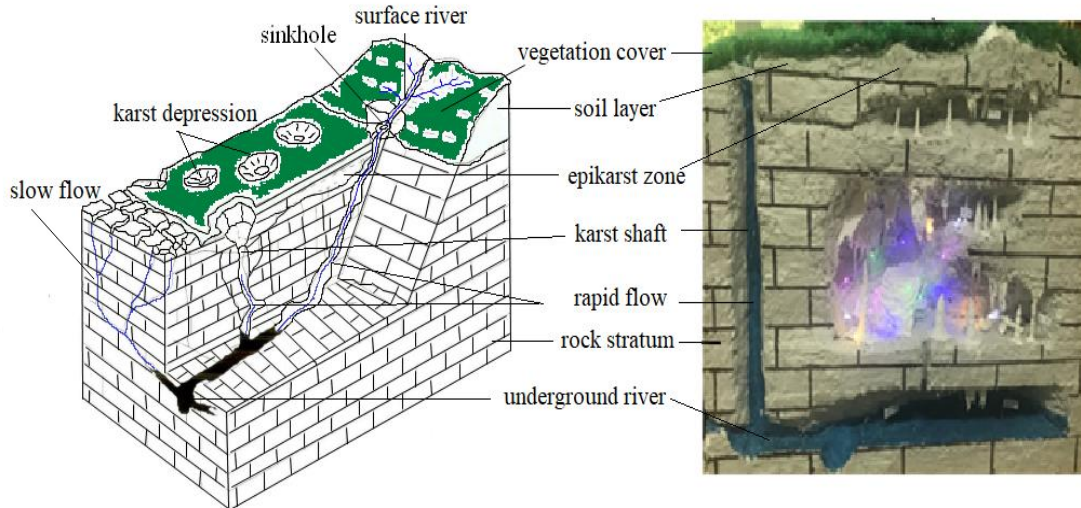
997

998   Figure 3 Spatial structure of the KHRUs (Li et al.,2021).
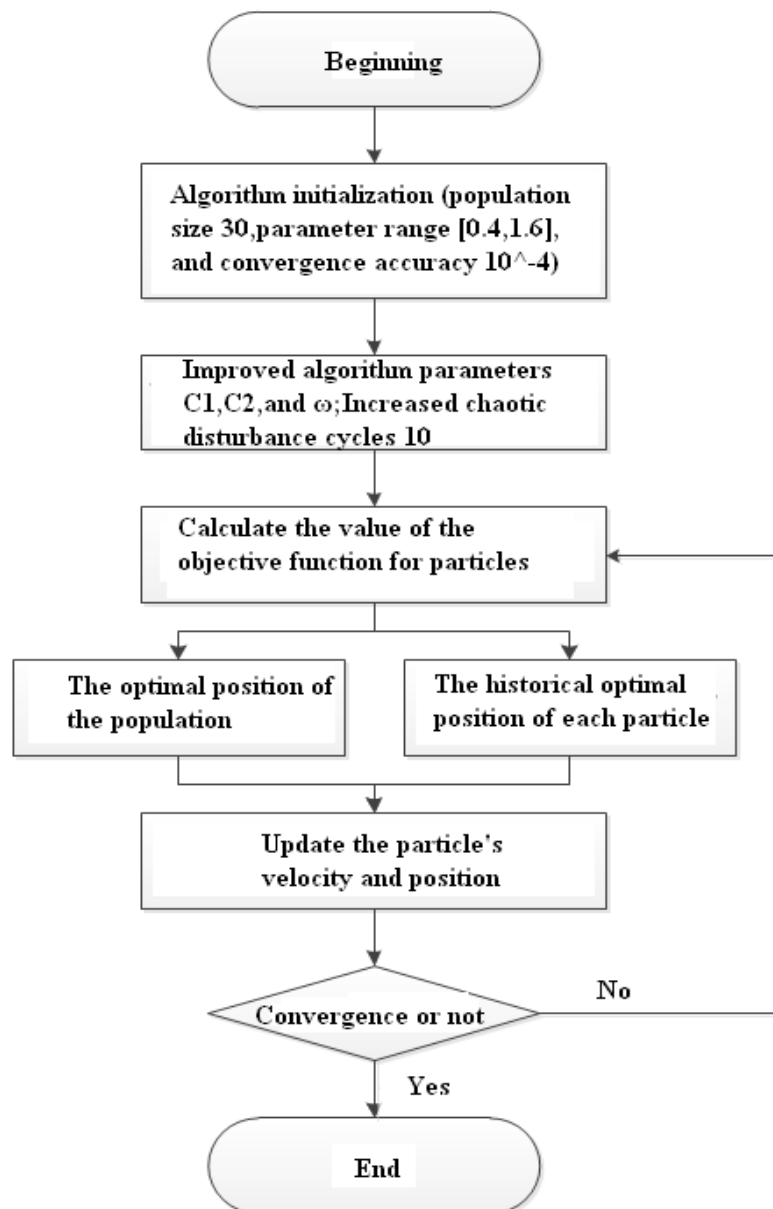
999

1000   Figure 4 Algorithm flow chart of the IPSO.
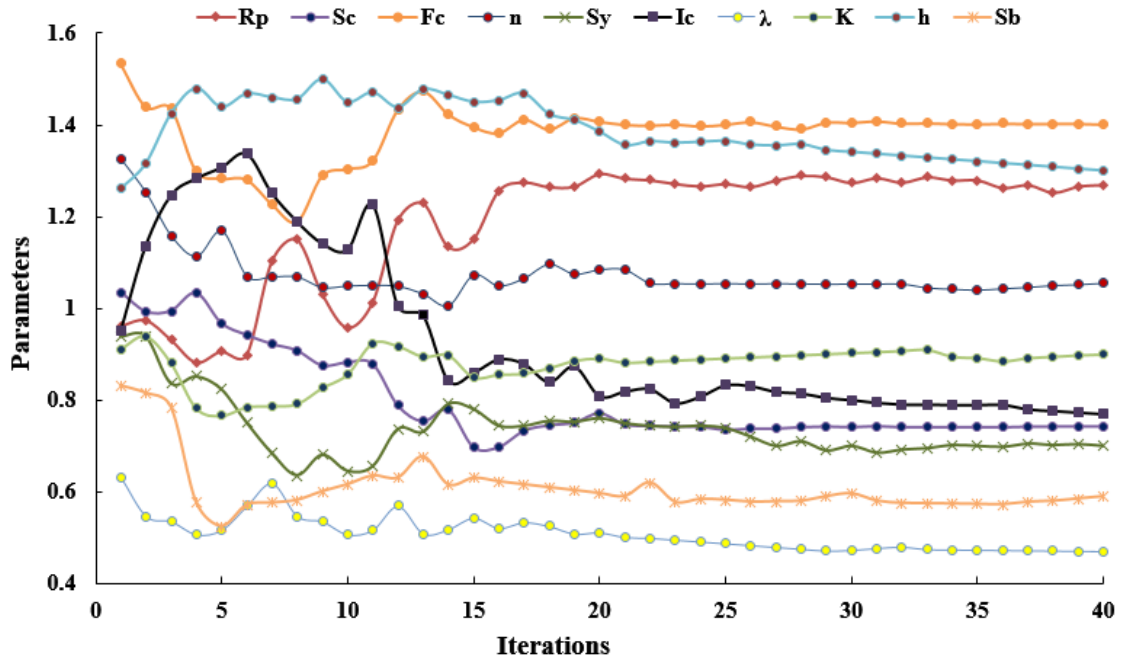
1001

1002   Figure 5 Iteration process of parametric optimization.
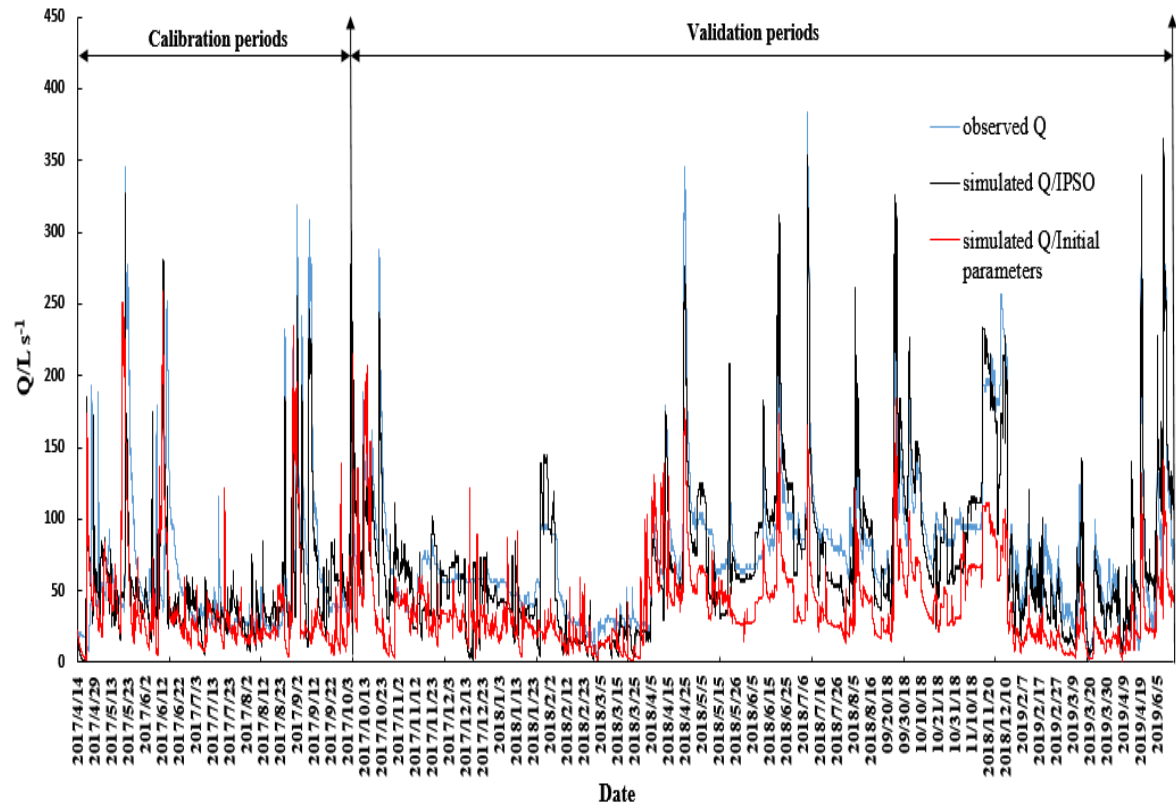
1003

1004   Figure 6 Flow simulation results of QMG model based on parameter optimization.
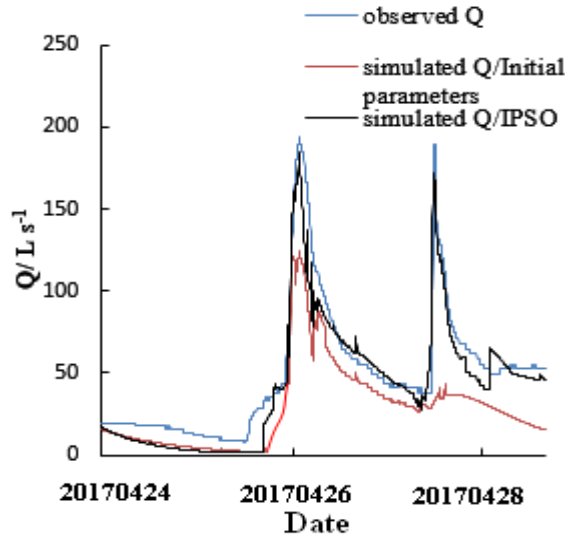
1005

1006   a. flood 201704240800   b. flood 201705081600
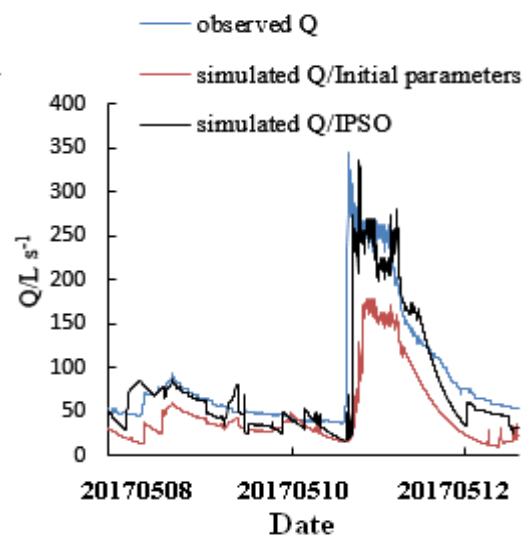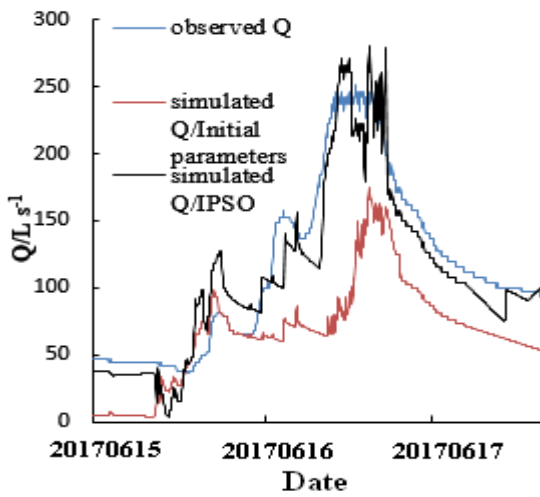
1007

1008   c.flood 201706151800   d. flood 201707101530
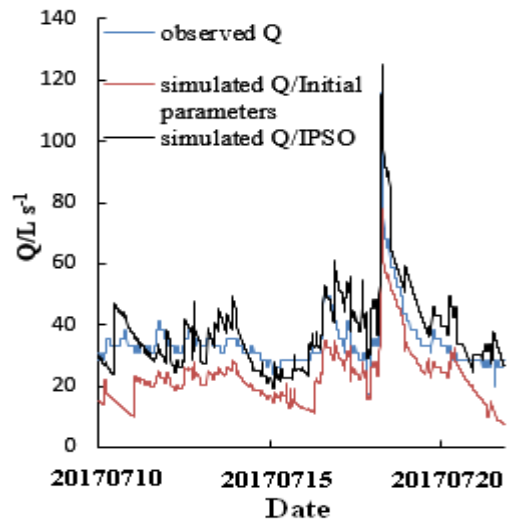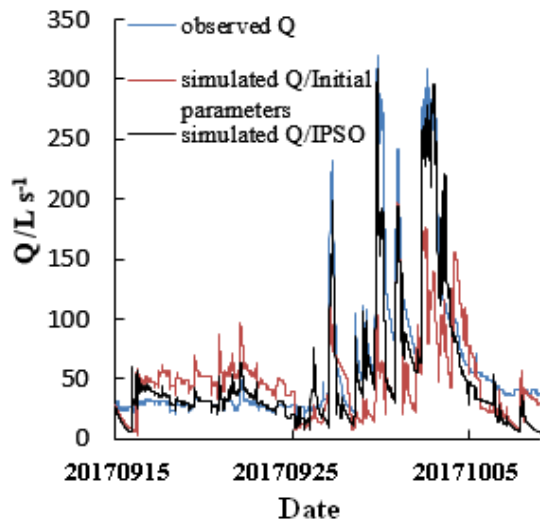
1009

1010   e.flood 201709151200   f.flood 201710081500
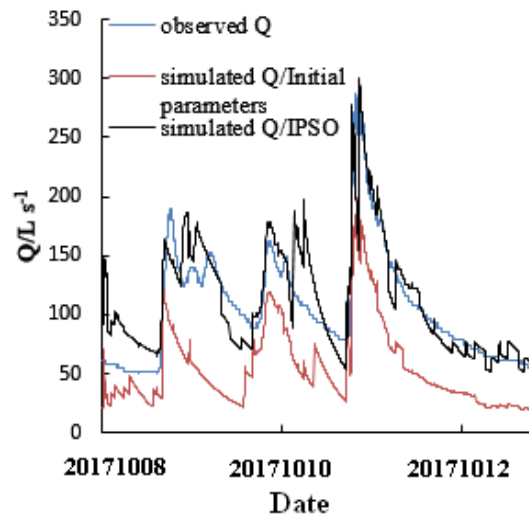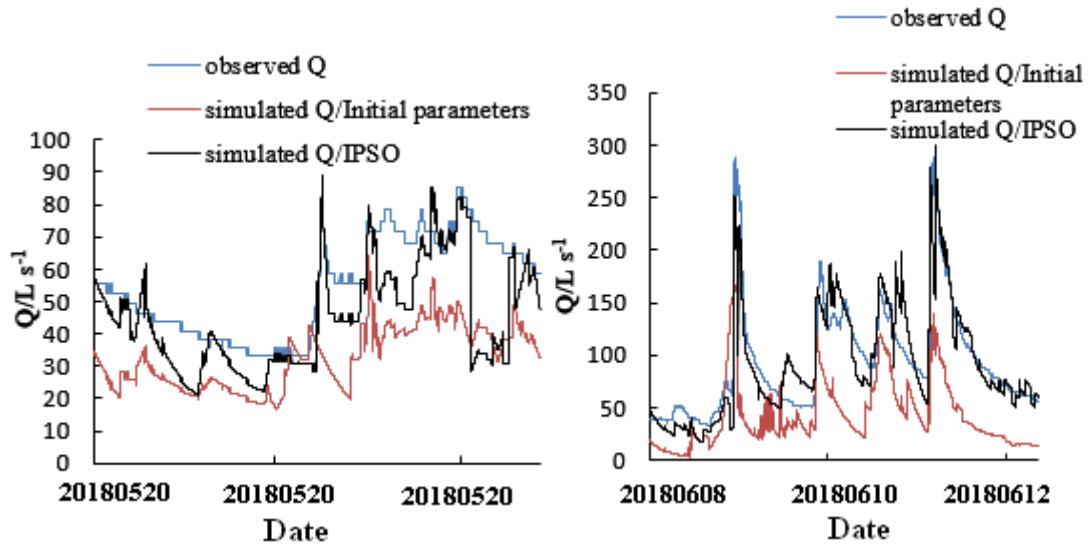
1011

1012      g.flood 201805201600        h.flood 201806081500
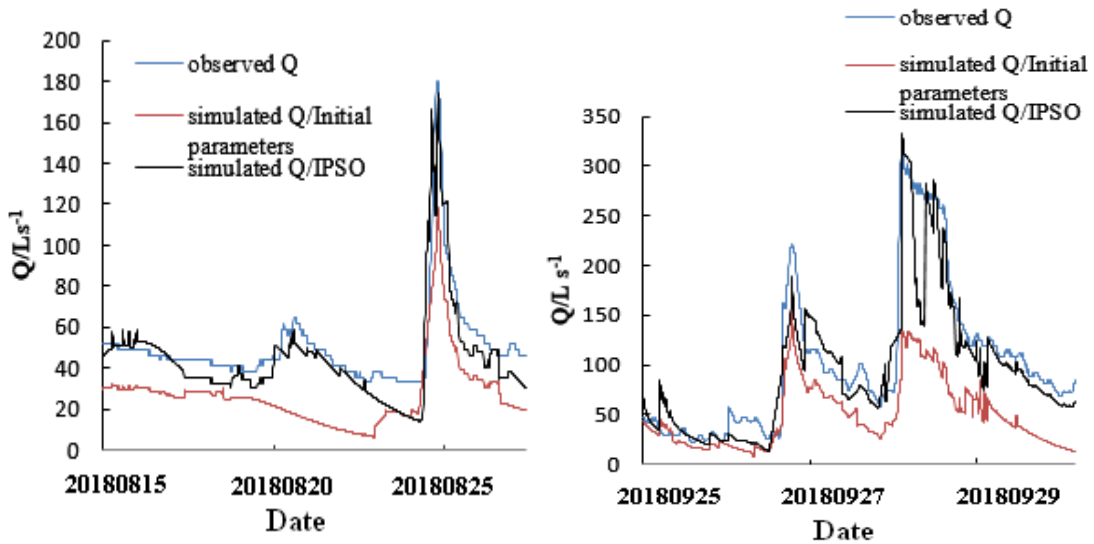
1013

1014      i.flood 201808151200       j.flood 201905251600

1015    Figure 7 Flood simulation effects based on initial and optimized parameters.